AGU PUBLICATIONS

JGR

Journal of Geophysical Research: Oceans

RESEARCH ARTICLE

10.1002/2014JC009953

Key Points:
- Intermediary circulation is effective at advecting shelf anomalies in the fjord
- An intrusion impacts water stratification at the glacier front and submarine melting
- Numerical results compare favorably to laboratory experiments with a similar setup

Correspondence to:
R. Sciascia,
sciascia@mit.edu

Citation:
Sciascia, R., C. Cenedese, D. Nicolì, P. Heimbach, and F. Straneo (2014), Impact of periodic intermediary flows on submarine melting of a Greenland glacier, *J. Geophys. Res. Oceans*, *119*, 7078–7098, doi:10.1002/2014JC009953.

Received 11 MAR 2014
Accepted 6 SEP 2014
Accepted article online 12 SEP 2014
Published online 24 OCT 2014

Impact of periodic intermediary flows on submarine melting of a Greenland glacier

R. Sciascia[1], C. Cenedese[2], D. Nicolì[3], P. Heimbach[1], and F. Straneo[2]

[1]Department of Earth, Atmospheric, and Planetary Sciences, Massachusetts Institute of Technology, Cambridge, Massachusetts, USA, [2]Department of Physical Oceanography, Woods Hole Oceanographic Institution, Woods Hole, Massachusetts, USA, [3]Department of Environmental Engineering, Università di Roma "Sapienza," Roma, Italy

Abstract The submarine melting of a vertical glacier front, induced by an intermediary circulation forced by periodic density variations at the mouth of a fjord, is investigated using a nonhydrostatic ocean general circulation model and idealized laboratory experiments. The idealized configurations broadly match that of Sermilik Fjord, southeast Greenland, a largely two layers system characterized by strong seasonal variability of subglacial discharge. Consistent with observations, the numerical results suggest that the intermediary circulation is an effective mechanism for the advection of shelf anomalies inside the fjord. In the numerical simulations, the advection mechanism is a density intrusion with a velocity which is an order of magnitude larger than the velocities associated with a glacier-driven circulation. In summer, submarine melting is mostly influenced by the discharge of surface runoff at the base of the glacier and the intermediary circulation induces small changes in submarine melting. In winter, on the other hand, submarine melting depends only on the water properties and velocity distribution at the glacier front. Hence, the properties of the waters advected by the intermediary circulation to the glacier front are found to be the primary control of the submarine melting. When the density of the intrusion is intermediate between those found in the fjord's two layers, there is a significant reduction in submarine melting. On the other hand, when the density is close to that of the bottom layer, only a slight reduction in submarine melting is observed. The numerical results compare favorably to idealized laboratory experiments with a similar setup.

1. Introduction

Greenland Ice Sheet mass loss provides a freshwater input to the oceans [*Bamber et al*., 2012] which, at present, accounts for one quarter of global sea level rise [*Shepherd et al*., 2012]. The acceleration and retreat of marine-terminating glaciers over the last decade [*Stearns and Hamilton*, 2007; *Howat et al*., 2007, 2008] are responsible for about half of this loss [*Rignot and Kanagaratnam*, 2006; *van den Broeke et al*., 2009] and evidence suggests that the ocean plays a crucial role [*Vieli and Nick*, 2011; *Straneo et al*., 2013; *Straneo and Heimbach*, 2013]. One of the proposed chain of events used to explain outlet glacier's retreat starts with subsurface warming of waters around Greenland, leading to increased submarine melting that ultimately impacts glacier stability (i.e., thinning, ungrounding, increased calving, and terminus retreat) [*Holland et al*., 2008; *Vieli and Nick*, 2011; *Straneo et al*., 2013; *O'Leary and Christoffersen*, 2013]. To improve our understanding of past Greenland outlet glacier variability and its future evolution, submarine melting and its controlling processes and parameters need to be better understood. However, this problem poses challenges both from an observational and modeling point of view.

In Greenland, tidewater glaciers terminate in deep narrow fjords that act as conduits between the glaciers and the continental shelf waters [*Straneo et al*., 2012]. The buoyancy-driven circulation generated by the glacier through the discharge of surface runoff at depth [*Chu et al*., 2009; *Das et al*., 2008] and submarine melting influences the near-glacier dynamics [see *Straneo and Cenedese*, 2014, for a review]. When the glacier (buoyancy)-driven circulation is the dominant circulation in the fjord, the heat transport to the glacier, responsible for its submarine melting, is expected to be in the form of an estuarine-like circulation [*Rignot et al*., 2010; *Motyka et al*., 2011], similar to that of Alaskan tidewater glaciers [*Motyka et al*., 2003, 2013].

At the glacier front, a buoyant plume composed of glacial meltwater and entrained ambient waters develops. The plume is forced by two distinct glacial meltwaters: subglacial discharge and submarine melting.

Herein, by subglacial discharge we refer to the fraction of surface glacier melting that is discharged at its base, and by submarine melting the melting of the glacier's front immersed in water. In the presence of only one ambient water mass, the plume, lighter than the ambient water, rises vertically near the glacier front and feeds a thin fast current of freshwater moving away from the glacier at the ocean's free surface. Entrainment in the buoyant plume generates a thick slow flow of ambient waters at depth moving toward the glacier. When two or more water masses are present [*Azetsu-Scott and Tan*, 1997; *Holland et al*., 2008; *Straneo et al*., 2010, 2012], the rising buoyant plume can move away from the glacier at the free surface and/or at an intermediate depth, depending of the plume's buoyancy forcing [*Sciascia et al*., 2013]. Observations [*Straneo et al*., 2011], laboratory experiments [*Huppert and Josberger*, 1980], and numerical simulations [*Sciascia et al*., 2013] have shown that the presence of multiple water masses in the fjord can result in this more complex "multiple cells" circulation. This glacier-driven circulation and the dynamics at the ice-ocean interface have been explored using both one-dimensional models based on the theory of buoyant plumes [*Hellmer and Olbers*, 1989; *Jenkins*, 1991, 2011], and more complex high-resolution ocean general circulation models [*Xu et al*., 2012; *Sciascia et al*., 2013; *Xu et al*., 2013].

However, the glacier-driven circulation may not be the only relevant mode of the fjord circulation [*Straneo and Cenedese*, 2014]. Data from two major Greenland glacial fjords, where Helheim and Kangerdlugssuaq Glaciers terminate, indicate that shelf driven flows, known as intermediary flows, may play a major role in fjord dynamics [*Straneo et al*., 2010; *Sutherland and Straneo*, 2012; *Jackson et al*., 2014]. In these two fjords, intermediary flows are found to be driven mainly by the halocline displacement at the mouth of the fjord due to the intense alongshore (e.g., Northeasterly) wind events [*Jackson et al*., 2014] observed throughout the year, but more frequently [*Moore and Renfrew*, 2005] during winter. Although upwelling/downwelling wind events are one of the most common forcing of intermediary flows, the definition given by *Stigebrandt* [1990] states that any density variations on the continental shelf, near the mouth of the fjord, can induce a horizontal pressure gradient in the fjord which, in turn, drives a baroclinic intermediary circulation. Thus, it can be assumed that a range of different forcings external to the fjord/glacier system (e.g., tides, coastally trapped currents, shelf winds, eddies) can generate density variations at the mouth of the fjord.

Klinck et al. [1981] explored the role of along and across-fjord wind events on fjord circulation. The geostrophic alongshore currents, generated by alongshore shelf winds, control the free surface and the halocline depth variation at the mouth of the fjord, and as a result, strongly affect the circulation in the fjord.

For example, by depressing the halocline at the mouth of the fjord and the consequent rising of the free surface, the Northeasterly wind events will drive in the fjord a baroclinic outflow (i.e., toward the fjord's mouth) of waters at depth and an inflow (i.e., toward the glacier front) of waters in the upper layer. When the wind ceases, the continental shelf will return to its prewind state and the fjord will reverse its circulation. It is worth noting that the described mechanism is a purely baroclinic flow, and the free surface slope is a consequence of the halocline depth variation *Klinck et al*. [1981]. *Arneborg* [2004] investigated the influence of a new water mass generating an intermediary circulation and intruding into the fjord in the intermediate layer. Inside the fjord, in the first half cycle, the rising of the halocline is due to an inflow of relatively warm salty water below the halocline, and a corresponding outflow of surface water. In the second half cycle, the halocline descends and the water below the halocline moves out of the fjord, and new water enters the fjord into the upper layer.

The intermediary circulation generates an exchange flow with the shelf and is responsible for the renewal of waters inside the fjord. The advection of waters from the shelf to the upper fjord occurs at a much faster rate than for a glacier-driven circulation. There is evidence that intermediary circulations are an important mode of circulation and affect the heat transport to the glacier for at least some fjords in Greenland [*Jackson et al*., 2014]. However, their impact on the buoyant plume and the associated submarine melting has not been previously studied. Assessing, from field observations, the relative impact of different circulations, e.g., glacier-driven and intermediary, on submarine melting can be a challenging task.

Here we investigate the impact of periodic density variations at the mouth of the fjord on the submarine melting and the fjord's dynamics using idealized laboratory experiments and a two-dimensional (2-D), high-resolution, nonhydrostatic ocean general circulation model (GCM) with a thermodynamical melt rate parameterization of the vertical glacier front. The numerical model configuration consists of an idealized

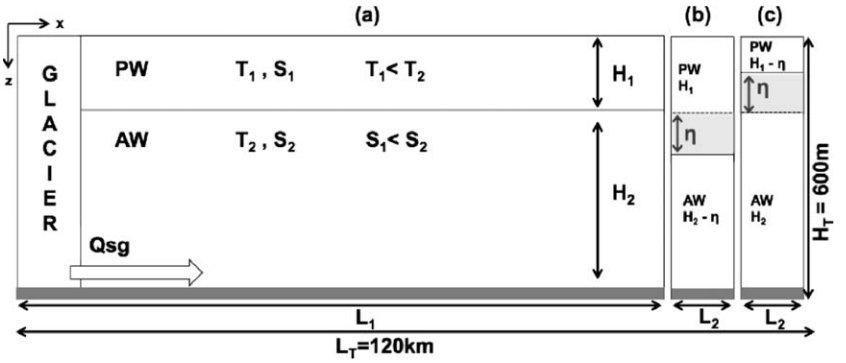

Figure 1. Numerical model setup with the glacier front on the left side and fjord's mouth on the right side of the domain. (a) Fjord "no-forcing" state. This configuration is used both as the fjord's initial condition for the length L_1 and as a pre/post density variation boundary condition at the mouth of the fjord (L_2); boundary conditions at the mouth of the fjord (L_2=2 km) for a (b) downward and (c) upward density variation applied in the light gray region, respectively (see section 2.2, for details).

version of the Sermilik Fjord/Helheim Glacier system in southeast Greenland. Observations provide the initial and boundary conditions for the temperature and salinity of fjord. In this study, we focus solely on intermediary circulations driven by periodic density variations at the mouth of the fjord. It should be noted that this kind of intermediary circulation is different from that forced by a periodic halocline displacement at the mouth of the fjord driven by upwelling/downwelling wind events. The latter advects waters into the fjord that have properties identical to either the top or bottom layers, while the intermediary circulation investigated in this study advects waters that have properties (e.g., temperature (T) and salinity (S)) that are in between those found in the top and bottom layers. In particular, this study focuses on two types of forcing achieved through two different density variations. First, we focus on a sinusoidal variation of T and S at the mouth of the fjord that produces an intrusion with averaged properties intermediate between those found in the two layers (sinusoidal forcing). Second, we investigate a top-hat variation of T and S that produces intrusions with properties that are close to those of the bottom layer (top-hat forcing). We stress that the problem addressed here does not focus on the advection of property anomalies that do not fall in between those of the top and bottom layers in the fjord. For example, the advection of waters with temperature warmer/colder than those found in the fjord could affect submarine melting in a different way than simulated in this study. The results of the present study are therefore relevant to that class of periodic intermediary circulations which advect waters into the fjord with properties (e.g., temperature) intermediate between those found in the fjord. Both summer and winter conditions are investigated using the numerical model, and only winter conditions using the laboratory experiments.

The numerical model and laboratory configurations are described in sections 2 and 3, respectively. The intermediary circulation is discussed in section 4. The main numerical findings for the sinusoidal forcing are presented in section 5. Sections 6 and 7 illustrate the results of the laboratory experiments and numerical simulations, respectively, for the top-hat forcing. Summary and conclusions are drawn in the final section.

2. Numerical Model Setup

To investigate the impact of a periodically forced intermediary circulation on submarine melting and the fjord's dynamics, we use the same model setup as *Sciascia et al*. [2013] and apply different boundary conditions at the fjord's mouth. We consider a high-resolution nonhydrostatic 2-D setup (Figure 1) of the ocean general circulation model MITgcm (http://mitgcm.org) [*Marshall et al*., 1997a, 1997b; *Adcroft et al*., 2004] with a melt rate parameterization at the vertical glacier front. Previous simulations [*Sciascia et al*., 2013] have shown that three-dimensional (3-D) simulations are dynamically equivalent to 2-D simulations provided that the forcing applied (e.g., subglacial discharge) is 2-D. Hence, we have chosen a 2-D setup with a reduced computational cost to enable a large number of simulations. The configuration is chosen to broadly match the properties of Helheim Glacier and Sermilik Fjord, one of the major fjord/glacier systems in southeast Greenland (66°N, 38°W) [*Straneo et al*., 2010]. The real fjord is about 100 km long, 6 km wide, and with a depth varying from 900 m at the mouth to 600 m at the glacier front [*Schjøth et al*., 2012]. Two

Table 1. Value of Dimensional Parameters Used in Each Simulation[a]

Experiment	Qsg ($m^3\ s^{-1}$)	t_{IC} (d)	η (m)	$\overline{smr}$ ($m\ yr^{-1}$)
WIN	0			70
SUM	4.3			738
IC	0	2	+ 50	0
WINup	0	1–10	+(10–90)	30–44
WIN2u50	0	2	+50	34
WIN2d50	0	2	−50	24
WINdw	0	1–10	+(10–90)	11–40
SUMup	4.3	1–10	+(10–90)	755–820
SUM2u50	4.3	2	+50	783
SUM2d50	4.3	2	−50	716
SUMdw	4.3	1–10	−(10–90)	675–740
WINth	0	(t_B) 1.5–26	+10	55–58

[a]Horizontal viscosity $\nu_H = 2.5 \times 10^{-1} m^2 s^{-1}$, vertical viscosity $\nu_V = 10^{-3} m^2 s^{-1}$, horizontal diffusivity $k_H = 2.5 \times 10^{-1} m^2 s^{-1}$, vertical diffusivity $k_H = 2 \times 10^{-5} m^2 s^{-1}$, $\Delta z = \Delta y = 10m$ and $\Delta t = 5$ s, PW temperature $T_1 = -1.5°C$, AW temperature $T_2 = 4°C$, PW salinity $S_1 = 32.9$ psu, AW salinity $S_2 = 34.6$ psu, PW thickness $H_1 = 150$ m , AW thickness $H_2 = 450$ m, (see section 2.3 for details). See *Sciascia et al.* [2013] for a complete description of the simulations WIN and SUM.

additional tidewater glaciers contribute to the total freshwater flux of Sermilik Fjord. However, their contribution is small compared to that of Helheim Glacier. Moreover, the simplified 2-D setup does not allow to capture the complex circulation patters resulting from multiple tidewater glaciers. Hence, in this study, we consider only the Helheim Glacier/Sermilik Fjord system. The Rossby radius of the deformation and fjord's width are approximately equal. Hence, we expect rotational effect to be small and changes in water properties to occur mostly in the along-fjord direction [*Straneo et al.*, 2010; *Sutherland et al.*, 2014].

We represent the terminus of Helheim Glacier as a $H_T = 600$ m vertical wall, and Sermilik Fjord as a two-dimensional $L_T = 120$ km long and 600 m deep fjord with a 10 m uniform vertical resolution and a telescopic horizontal resolution going from 10 m at the glacier front to 500 m at the mouth of the fjord. The resolution in the y direction (Δy) is one grid cell of 10 m. Subgrid processes are parameterized by a Laplacian eddy diffusion of temperature (κ_T), salinity (κ_S), and momentum (ν) with grid-rescaled constant coefficients. For the processes considered here, turbulence dominates diffusive and viscous processes. Hence, $\kappa = \kappa_T = \kappa_S$ and ν are of the same order of magnitude and the horizontal Prandtl number, Pr, is equal to one. As discussed in detail by *Sciascia et al.* [2013], the magnitude of the diffusive and viscous coefficients is chosen to correctly represent the entrainment processes within the buoyant plume that are not resolved at the current grid spacing. A list of the parameters used in the simulations is given in Table 1. The boundary conditions of the model are free surface at the top, no-slip rigid boundaries at the bottom and on the left side of the domain (i.e., glacier front). A sponge layer at the open boundary on the right side of the domain is used to impose the periodic density variation at the fjord's mouth (see section 2.2, for details). The melt rate parameterization of the ice front is based on the three-equation model [*Hellmer and Olbers*, 1989; *Holland and Jenkins*, 1999] with velocity-dependent turbulent transfer coefficients. This parameterization has been previously used in the MITgcm to model submarine ice shelf melting in Antarctica [*Losch*, 2008; *Heimbach and Losch*, 2012; *Schodlok et al.*, 2012; *Dansereau et al.*, 2013], and to evaluate submarine melting in Greenland tidewater glaciers [*Xu et al.*, 2012; *Sciascia et al.*, 2013; *Xu et al.*, 2013].

2.1. Initial Conditions—Seasonal Variability

We consider two seasonally variable initial conditions. As argued in recent studies, one of the largest seasonal controls on the fjord's circulation and submarine melting is subglacial discharge (Qsg) [*Motyka et al.*, 2003; *Jenkins*, 2011; *Xu et al.*, 2012; *Sciascia et al.*, 2013]. In summer, a fraction of the surface runoff reaches the bed of Greenland's glaciers and is discharged at depth into the fjord [*Andreasen*, 1985; *Zwally et al.*, 2002; *Catania et al.*, 2008; *Das et al.*, 2008]. Geothermal melting and frictional melting at the base of the glacier are present throughout the year but are a small fraction (∼8%) of the total subglacial discharge [*Mernild et al.*, 2010]. *Sciascia et al.* [2013] showed that for small values of subglacial discharge the leading order dynamics is similar to that observed in the absence of a subglacial discharge forcing. Thus, we consider a winter regime without subglacial discharge and a summer regime in which the subglacial discharge is confined to the bottom of the domain.

We use the same method as *Sciascia et al.* [2013] to obtain 2-D rescaled subglacial discharge rates from the *Andersen et al.* [2010] summer estimate of $Qsg^* = 174\ m^3\ s^{-1}$. We infer a summer regime with $Qsg = 4.35\ m^3\ s^{-1}$ equivalent to a subglacial discharge Qsg^* occurring not from the entire width of the glacier but from a single opening 400 m wide and 20 m high (i.e., $\frac{Qsg^*}{A^*} = \frac{Qsg}{A}$, where $A^* = 400 \times 20\ m^2$ and $A = 10 \times 20\ m^2$ are the real and modeled area where the subglacial discharge enters the fjord). The

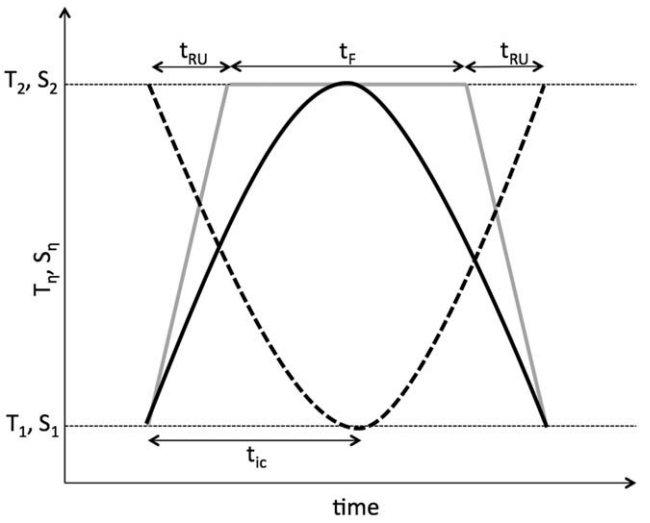

Figure 2. Schematic of the temperature, T_η, and salinity, S_η, time evolution applied as a boundary condition in the sponge layer at the mouth of the fjord in a volume $V_\eta = L_2 \times \eta \times \Delta y$ (light gray region in Figures 1b and 1c). The black solid line represents an upward sinusoidal forcing, the black-dashed line a downward sinusoidal forcing, and the gray line an upward top-hat forcing.

subglacial discharge is at the freezing temperature for the given depth, with zero salinity, and with the initial horizontal velocity computed from the total discharge $u_{Qsg} = Qsg/A$.

In both seasons, we neglect the ice mélange. The highly simplified nature of the 2-D numerical model is not appropriate to explore the role of ice mélange on fjord dynamics and submarine melting. Ice mélange has a 3-D spatial distribution and it is highly sensitive to atmospheric forcing, i.e., winds. Hence, a more realistic 3-D setup would be required.

Water properties inside Sermilik Fjord also vary seasonally. Hydrographic surveys [*Straneo et al*., 2010, 2011] have shown that Sermilik Fjord is filled with two water masses: cold and fresh Polar Water (PW) overlaying warm and salty Atlantic Water (AW). Winter profiles show a two-layer stratification of temperature and salinity, whereas in summer the stratification is more complex [*Straneo et al*., 2011]. The differences in summer/winter water properties influence the submarine melting, but their effect is secondary compared to the presence/absence of subglacial discharge. Simulations with subglacial discharge using winter or summer water properties have shown the same leading order dynamics [*Sciascia et al*., 2013]. For simplicity, we initialize the model in both seasons with a winter idealized two-layer stratification in which the temperature and salinity of each layer are equal to the averaged winter observations in each layer and with the interface between the two layers located at 150 m (Table 1).

2.2. Boundary Conditions—Periodic Density Variation

To model the horizontal pressure gradient generated by a density variation at the mouth of the fjord and the induced baroclinic intermediary circulation, we consider two different boundary condition scenarios, sinusoidal and top-hat forcings (Figure 2), applied within a sponge layer, of width L_2, at the mouth of the fjord. The density variation is applied in a forcing volume $V_\eta = L_2 \times \eta \times \Delta y$ at the mouth of the fjord (light gray region in Figures 1b and 1c).

In the upward "sinusoidal" density variation scenario (Figures 1b and 2, black solid line), the temperature (T_η) and salinity (S_η) in the forcing volume V_η at the mouth of the fjord change following the black solid line in Figure 2 with a forcing time (t_{IC}). A similar perturbation is applied in the downward sinusoidal density variation scenario (Figures 1b and 2, black solid line). The wording "upward" ("downward") is used to indicate that V_η is located above (below) the PW/AW interface and consequently the PW (AW) layer depth is $H_1 - \eta$ ($H_2 - \eta$) while keeping H_T constant, as shown in Figure 1c (Figure 1b). We have considered a wide range of values for η, from 10 to 90 m, and the forcing time t_{IC}, from 1 to 10 days. The forcing time t_{IC} is equivalent to half a period (Figure 2, black lines).

The second scenario is the "top-hat" forcing in which the temperature and salinity in the volume V_η vary following the gray line in Figure 2. In this case, the forcing time ($t_B = t_{RU} + t_F$) is the sum of the ramp-up time, t_{RU}, and t_F, the time in which the temperature and salinity are kept constant to T_2, S_2. Only upward top-hat density variation with $\eta = 10$ m will be considered (Figure 1c). This scenario is equivalent to the forcing used in the laboratory experiment (see section 3).

The two scenarios described above represent different possible external forcings on the continental shelf. While in the sinusoidal scenario, the averaged properties at the mouth of the fjord are intermediate between those of the PW and AW, in the top-hat scenario the averaged properties are similar to those of

the bottom AW. We assume that these density variations at the mouth of the fjord are due to changes originating outside the fjord. The mechanisms that may cause these density variations upstream of the fjord are not the focus of this study, but possible mechanisms include shear mixing, strong wind events, and eddies. Although the production of a new water mass with properties in between those of the AW and PW has not been observed yet at the mouth of Sermilik Fjord, the above seem plausible mechanisms for the generation of a density variation upstream of the fjord.

In both scenarios, the boundary conditions at the mouth of the fjord are defined independently of the flow inside the fjord (see section 4). As noted by *Klinck et al*. [1981], this is an ill-posed problem since the density variation at the mouth of the fjord cannot be specified consistently with the flow inside the fjord. Nevertheless, we assume that the above configurations are good approximations of the intermediary circulation induced in the fjord by a density variation at the fjord's mouth.

2.3. Model Simulations

We conducted a series of simulations to investigate the effects of a periodically forced intermediary circulation on submarine melting and fjord dynamics for winter and summer conditions. The simulations are briefly described here and summarized in Table 1.

Intermediary Circulation Simulation—IC. We explore the effect of a sinusoidal density variation at the fjord's mouth on fjord circulation. We consider an upward sinusoidal forcing with a 2 days forcing time, $\eta = +50$ m, and the idealized fjord geometry, but without a thermodynamically active glacier front.

Sensitivity to Upward Sinusoidal Forcing—WINup and SUMup. We explore, for winter (WINup) and summer (SUMup) conditions, the effects of upward sinusoidal density variations (Figure 2, black solid line). At the fjord's mouth (L_2), we force a volume V_η (Figure 1c), where η ranges from $+10$ to $+90$ m, with 20 m increments. For each simulation, we also vary the forcing time (t_{IC}) from 1 to 10 days (1, 2, 4, 6, 8, and 10 days). We consider, as reference simulations, a winter (WIN2u50) and summer (SUM2u50) configuration, with $\eta = +50$ m and $t_{IC} = 2$ days.

Sensitivity to Downward Sinusoidal Forcing—WINdw and SUMdw. Same as WINup and SUMup, but for downward sinusoidal density variations (Figures 1b and 2, black-dashed line).

Sensitivity to Upward Top-Hat Forcing—WINth. We explore, for winter conditions, the effects of a top-hat forcing (Figure 2, gray line) with $\eta = +10$ m and a variable t_B from 1.5 to 26 days.

Winter Simulation—WIN. This simulation, also carried out in *Sciascia et al*. [2013], is used as a control simulation for the winter condition. The fjord has winter water properties and no subglacial discharge.

Summer Simulation—SUM. This simulation with winter water properties and a steady subglacial discharge $Qsg = 4.3$ m^3 s^{-1} is used as a control simulation for the summer condition [see *Sciascia et al*., 2013, for a detailed description).

The simulations are compared in terms of simulated hydrographic properties, velocity fields, submarine melting at a given depth, $smr(z)$ (m yr^{-1}), and the vertically averaged submarine melting defined as $\overline{smr} = \frac{1}{H_T}\int_{-H_T}^{0} smr(z)dz$ (m yr^{-1}). Note that this definition averages the submarine melting over the entire water column depth.

To estimate the time-mean of the vertically averaged submarine melting ($\overline{smr}$), we average the time series over the maximum number of complete periods of variability.

3. Laboratory Experiments Setup

The laboratory experiments are conducted in a rectangular tank, 150 cm long, 15 cm wide, and 30 cm deep (Figure 3). The tank is insulated using triple paneled glass filled with argon. It is located in a cold room with temperature T_{air} that is kept approximately constant during each experiment and varies between 2.9 and 3.9°C for the different experiments. A two-layer stratification is produced by first adding a bottom layer of depth $H'_2 = 18$cm of warmer, $T_2 \approx 3$°C, saltier, $S_2 \approx 34$psu, water. Yellow food dye is added to the bottom layer. When the bottom layer comes to rest, cooler, $T_1 \approx 0.5$°C, fresher, $S_1 \approx 32$ psu, water is added from a reservoir through a float (in order to minimize mixing at the interface between the two layers) to form a second layer of depth $H'_1 = 5$ cm. The total water depth in the tank is $H'_T = 23$ cm. Temperatures, salinities, and

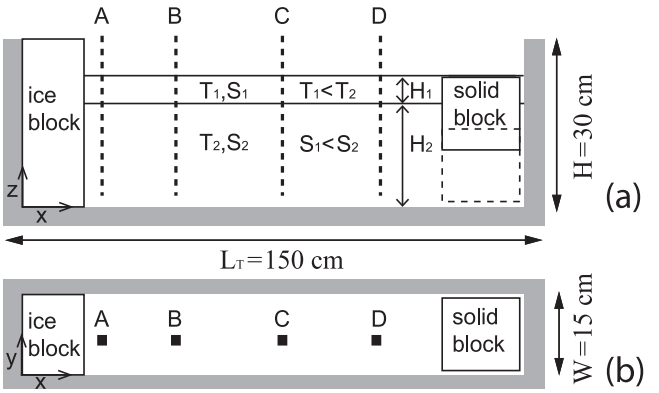

Figure 3. Laboratory experimental apparatus: (a) side view and (b) top view. The vertical dashed lines indicate the position of the conductivity-temperature probes located (A) 2, (B) 30, (C) 60, and (D) 90 cm away from the ice front. Not to scale.

depth of the two layers are selected to approximately match those observed in Sermilik Fjord in winter. The addition of the second layer causes a perturbation of the interface between the two layers, and the experiment starts only after this perturbations decays.

The glacier is represented by a deaired and dyed (blue) ice block ($L_i = 10$ cm, $W_i = 15$ cm, $H_i = 30$ cm) located at one end of the tank (Figure 3). The temperature of the ice at the beginning of the experiment is $T_{ice} \approx -25^{\circ}$C and within approximately 1 h from positioning the ice block in the tank it reaches a constant value $T_{ice} \approx -1.6^{\circ}$C. After positioning the ice block in the tank, the total water depth is $H_T = 24.64$ cm, and the bottom and top layer depths are $H_2 = 19.28$ cm and $H_1 = 5.36$ cm, respectively. A digital camera is used to take digital pictures of the ice front position every 5 min. By analyzing these pictures, the time evolution of the submarine melting is estimated at different depths. The ice block face in contact with the water melts approximately in a 2-D fashion, however, the digital pictures revealed a slight inhomogeneity of the submarine melting in the y direction. Hence, the submarine melting is estimated as the mean between its maximum and minimum value for any given experiment, and the maximum and minimum values represent the error bars of the estimate. In order to compare the laboratory parameters with the numerical parameters and those observed in nature, we nondimensionalize depth using H_2, and time using $t_g = 2L_T/U_g$, where U_g and L_T are the gravity wave velocity (section 4) and length of the domain, respectively. Nondimensional variables will be indicated with an asterisk.

The intermediary circulation is generated by the periodic vertical displacement of a solid block ($L_b = 15$ cm, $W_b = 15$ cm, $H_b = 15$ cm) at the end of the tank opposite from the ice (Figure 3). At the beginning of the experiment, the upper face of the solid block is positioned just below the free surface (Figure 3a, solid square) and consequently the lower face of the solid block is approximately 10 cm below the interface between the two layers. This configuration is chosen to minimize the mixing between the two layers that would occur if the solid block crosses the free surface or the interface between the two layers. During the experiment, the solid block moves first downward of 9 cm, i.e., from its initial position to a position in which it is completely immersed in the lower layer (Figure 3a, dashed square) and hence it moves a volume of water in the lower layer equal to $V' = 9 \times 15 \times 15$ cm^3. The vertical displacement of the solid block toward the bottom of the tank causes a horizontal displacement of the bottom layer toward the ice block and a consequent horizontal displacement of the top layer away from the ice block. By moving the solid block toward the top of the tank, an opposite circulation arises, i.e., the bottom (top) layer moves horizontally away from (toward) the ice block. The intensity of the circulation is proportional to the water mass displaced, i.e., the solid block volume, and to the vertical velocity of the solid block. This velocity is kept constant at approximately $v_b = 0.23$ cm s^{-1} and its magnitude cannot be increased without mixing considerably the two layers. Given this velocity, the ramp-up time is equivalent to $t_{RU} = 39$ s (Figure 2). The nondimensional ramp-up time for the laboratory experiments, $t_{RU}/t_g = 39$ s$/104$ s $= 0.37$, is equivalent to that of the numerical simulations, $t_{RU}/t_g = 24$ h$/65.6$ h $= 0.37$.

The time separating two consecutive movements of the solid block is defined as t_B and, similarly to the numerical simulations with a top-hat forcing, is the sum of the ramp-up time t_{RU} and t_F (Figure 2, gray line). During the consecutive movement, the solid bock returns to its initial position with its upper face positioned just below the free surface. The values of t_B for each experiment are listed in Table 2 and range between $0.4 \leq t_B/t_g \leq 14$, while for the top-hat numerical simulations $t_B^* = t_B/t_g$ varies between 0.5 and 9. The values of t_g for the numerical simulations and the laboratory experiments are 65.6 h and 104 s, respectively. Although the laboratory experiments investigate a larger range of values of this parameter, the forcing time of the laboratory experiments is comparable to that used in the numerical simulations. The

Table 2. Value of Dimensional Parameters Used in Each Experiment (see Section 3 for Details)[a]

Experiment	t_B (min)	S_1 (psu)	T_1 (°C)	S_2 (psu)	T_2 (°C)	T_{air} (°C)	t_{CT} (min)	$\overline{smr}$ (cm min^{-1})
1	0.00	31.9	1.1	34.1	3.0	3.6	1.0	0.0039
2	24.00	32.0	0.5	34.1	3.0	3.1	2.0	0.0044
3	12.00	32.1	0.9	34.1	3.0	3.6	24.0	0.0050
4	8.00	31.9	0.6	34.0	3.0	3.1	2.0	0.0049
5	6.00	32.1	0.4	34.3	3.1	3.4	12.0	0.0042
6	6.00	32.0	1.2	34.0	3.0	3.5	2.0	0.0049
7	3.33	32.0	0.8	34.1	3.1	3.9	13.3	0.0055
8	1.67	32.2	0.8	34.0	3.1	2.9	9.9	0.0046
9	1.67	32.0	0.5	34.2	3.0	3.1	10.0	0.0037
10	1.00	32.0	0.9	34.1	3.0	3.7	10.4	0.0046
11	1.00	32.0	0.5	34.2	3.0	3.2	10.4	0.0037
12	0.67	31.9	0.3	34.1	3.0	3.5	12.7	0.0043
13	0.67	32.0	0.9	34.0	3.0	3.8	12.7	0.0038
14	0.67	32.1	0.4	34.0	3.1	3.8	12.7	

[a]The depth of the PW and AW layers is kept constant for all the experiments $H_1 = 5.36$ cm, $H_2 = 19.28$ cm with the exception of experiment 8 in which $H_2 = 16.28$ cm.

movement of the solid block causes the interface to rise slightly of $\eta = 0.6$ cm, i.e., $\eta/H_{2(LAB)} = 0.03$, while for the top-hat numerical simulations $\eta/H_{2(NUM)} = 0.02$ where $\eta = 10$ m. For comparison, although with a different forcing, in the sinusoidal numerical simulations $t^*_{IC} = t_{IC}/t_g$ varies between 0.35 and 3.5 and $0.02 \leq \eta/H_{2(NUM)} \leq 0.2$.

A limitation of this experimental set up is the fact that the boundary conditions on temperature and salinity at the mouth of the fjord (i.e., near the solid block) cannot be kept constant. In other words, the waters in the two layers cannot be replenished and the glacially modified water slowly fills up the entire tank. However, the submarine melting is evaluated within the first 240 min of the experiment and we consider solely the submarine melting at 5 cm above the bottom, i.e., $smr_5 = smr(z = 5cm)$ (cm min^{-1}). Within the first 240 min, the glacially modified water, slowly filling the tank, is located well above 5 cm above the bottom ensuring that the submarine melting evaluated at this depth is not influenced by the glacially modified waters. When the submarine melting is not presented as a function of time, a 240 min averaging window is used.

Four temperature and conductivity probes are located at 2, 30, 60, and 90 cm, respectively, from the ice front. A motor is programmed to move the probes and acquire vertical profiles in the tank, the time interval between two consecutive vertical profiles is defined as $t_{CT,}$ and the values for each experiment are listed in Table 2. Measurements are taken only during the downward movement of the probes, which takes approximately 22 s, and the vertical spacing of the measurements is 0.1 cm. After the measurements are taken, the probes return to their resting position above the free surface. After the two-layer stratification is established and before the ice block is introduced in the tank, a vertical profile is acquired and used to calculate temperature anomalies. A measure of the horizontal velocity is obtained by dropping potassium permanganate crystals approximately 30 cm from the ice front. Digital movies of the purple streaks left behind the crystals are taken, in the vertical plane orthogonal to the horizontal motion, approximately 1 h after the experiment starts and for 10–20 min depending on the experiment. The analysis of the digital movies gives a measure of the evolution in time of the horizontal velocity at different depths.

Given the complexity of the experimental apparatus and measurements taken, the laboratory experiments investigate the influence of intermediary circulation on submarine melting only for winter conditions, i.e., in the absence of subglacial discharge. A total of 14 experiments with eight different values of t^*_B are conducted, including a reference experiment with no forcing. Two experiments are conducted for $t^*_B = 3.5$, 1.0, and 0.6 and three experiments for $t^*_B = 0.4$.

4. Model Results: Intermediary Circulation (IC)

The upward sinusoidal density variation in the volume V_η ($\eta = +50$ m) at the mouth of the fjord induces a horizontal pressure difference between the fjord interior and the mouth with the consequent onset of an intermediary circulation [*Stigebrandt*, 1990]. Two types of flow are established inside the fjord. The first is a gravity wave generated at the interface between the PW and AW layers. Its traveling speed can be estimated following *Benjamin* [1968]:

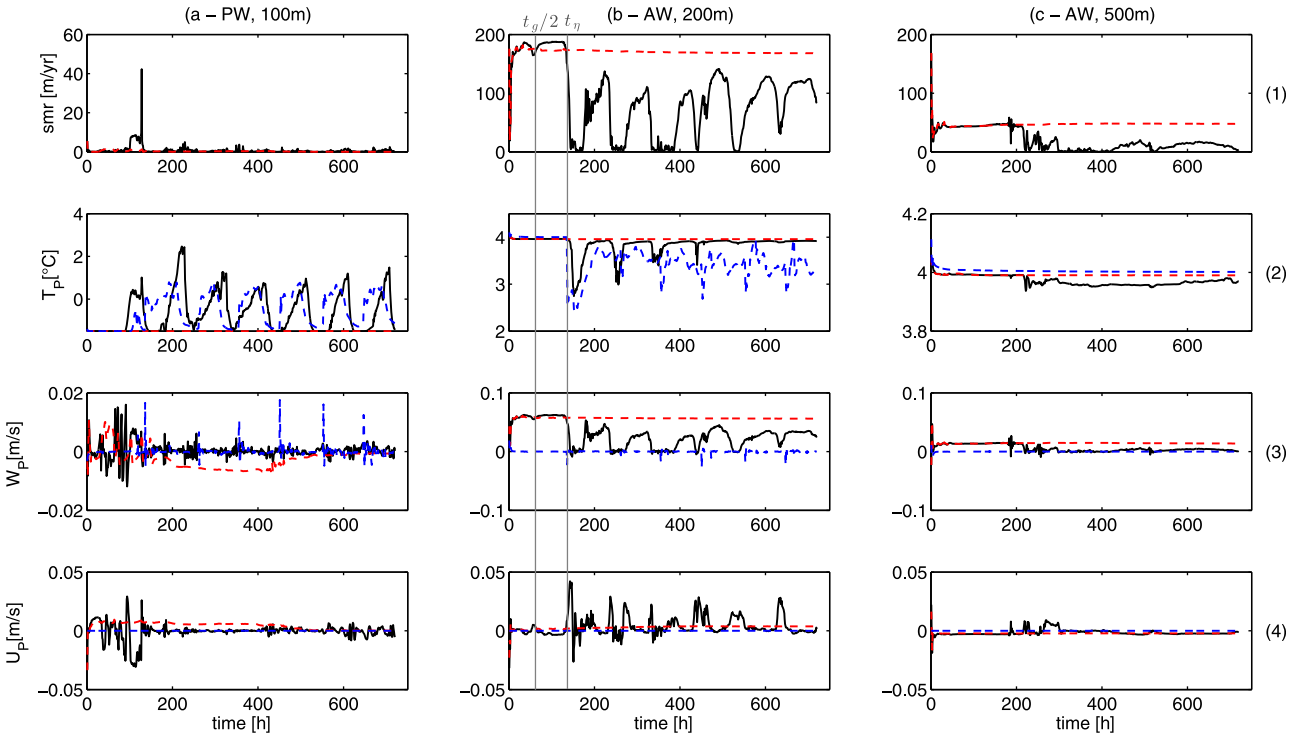

Figure 4. Winter intermediary circulation: (1) submarine melting at the glacier front, and (2) temperature, (3) vertical, and (4) horizontal velocity in the buoyant plume as a function of time for different depths: (a) 100 m (PW), (b) 200 m (AW), (c) 500 m (AW). Blue-dashed lines represent the IC model simulation, red-dashed lines the WIN control simulation, and black solid lines the WIN2u50 reference simulation. Note the different scales in Figures 4a–4c. Gray solid lines in Figure 4b, rows 1–4 indicate the theoretical arrival time of the gravity wave ($t_g/2$) and intrusion (t_η), see section 4.

$$U_g = \sqrt{g' \frac{H_1 H_2}{H_T}}, \tag{1}$$

where $g' = g(\rho_2 - \rho_1)/\rho_0$ is the reduced gravity and ρ_0 is a reference density. Equation (1) is valid if the velocities in the two layers are much smaller than the gravity wave speed, which is usually the case in the numerical simulations. This is the fastest velocity scale in the fjord with $U_g = 1$ m s^{-1}. The arrival time of the gravity wave at the glacier front is $t_g/2 = L_T/U_g = 32.8$ h. The gravity wave does not significantly alter the near glacier dynamics and induces a very small variability in the water properties near the glacier front (Figure 4, blue-dashed lines, not visible with this scale).

In addition to the gravity wave, the density variation in the volume V_η at the mouth of the fjord generates a new water mass that propagates within the fjord as a density intrusion located mainly above the PW/AW interface. We assume that the averaged density of this intrusion is intermediate between the PW and AW densities, i.e., $\rho_i = (\rho_2 + \rho_1)/2$, with a reduced gravity compared to the PW layer of $g_i' = g(\rho_i - \rho_1)/\rho_0$, and that the velocities of the waters above and below the intrusion are zero. Hence, the speed of this intrusion can be estimated considering that the density structure is symmetric around an imaginary line passing through the middle of the intrusion and then considering the intrusion of depth $\eta/2$ as a gravity current propagating into the PW layer. The speed of this gravity current is [*Benjamin*, 1968]:

$$U_\eta = \frac{1}{\sqrt{2}} \sqrt{g_i' \eta/2}. \tag{2}$$

This velocity is smaller than the gravity wave speed, $U_\eta = 0.24$ m s^{-1}, and the arrival time of the intrusion (t_η) at the glacier front is given by $t_\eta = L_T/U_\eta = 138.8$ h. The arrival time of the gravity wave ($t_g/2$) and intrusion (t_η) in the model are in good agreement with the theoretical arrival times estimated from equations (1) and (2) (Figure 4, gray lines). It is important to note that since the first baroclinic mode wave speed is larger ($=1$ m s^{-1}) than the intrusion speed ($=0.24$ m s^{-1} for $\eta = +50$ m), it should be responsible for the higher frequency variability observed inside the fjord. However, we expect the new water mass to be advected by the flow at the slower, intrusion speed. Hence, the larger influence of the intermediary circulation should be observed near the glacier after a time t_η.

The numerical results (see below and Figure 4) suggest that the new water masses generated by density variations at the fjord's mouth are advected by an intrusion propagating with a velocity given by equation (2). However, further studies are required to determine if and under which circumstances the above velocity is a good scaling for the advection of density anomalies by intermediary circulations in real fjords.

As the new water mass reaches and reflects from the glacier front, it modifies the ambient water stratification near the glacier. This modification is mainly due to the intrusion's water properties, intermediate between those in the fjord, and secondarily to some inevitable mixing occurring as the intrusion propagates and reflects from the glacier front. Hence, the PW (AW) near the glacier becomes warmer (colder) than in the WIN control simulation (Figures 4a and 4b, row 2, blue-dashed lines). On the other hand, the velocity distributions close to the glacier are not significantly modified by the arrival of the intrusion (Figures 4a and 4b, rows 3 and 4, blue-dashed line). Figure 4a, row 3, shows several peaks in the velocity field near the glacier front corresponding approximately to the arrival time of the intrusion. However, these are limited in duration and do not affect the submarine melting (Figure 4a, row 1). Hence, the intermediary circulation has a "thermodynamical" effect a strong influence on the temperature but a small one on the velocities near the glacier.

5. Model Results: Sinusoidal Forcing

5.1. Winter (WIN2u50)

For the sake of the following discussion, we briefly describe the dynamics of a purely glacier-driven fjord circulation. A detailed description is provided in *Sciascia et al.* [2013]. In winter, submarine melting gives rise to a relatively fresh buoyant plume composed of a mixture of glacial waters and entrained ambient waters that rises vertically along the glacier front. Two distinct plumes are observed, one generated by the melting of the upper 150 m, within the PW layer, that reaches the free surface, and a second plume, generated by the melting in the AW layer, that intrudes horizontally at the interface between the two layers. Velocities within the plumes are mainly vertical, while horizontal velocities generated by the entrainment processes become dominant outside the plumes.

The interaction between the plume and the new water mass transported by the intermediary circulation (WIN2u50) generates a different near glacier dynamics compared to that in the absence of the intermediary circulation (WIN) (Figure 4, black solid lines and red-dashed lines, respectively). For an upward sinusoidal forcing at the mouth of the fjord (Figure 1c), the intermediary circulation advects a new water mass, of approximately intermediate temperature between T_1 and T_2, that warms part of the top 150 m of the water column at the glacier front (Figure 4a, row 2). The submarine melting in the PW layer is slightly higher than in the control simulation (WIN) (Figure 5a). On the other hand, the new water mass advected by the intermediary circulation leads to a lower temperature in the upper part of the AW layer compared to the control simulation (Figures 4b, row 2, and 5b) with a decrease in submarine melting (*smr*) in the AW layer (Figure 5a).

This result can be explained by the "melt-driven convection" regime [*Jenkins*, 2011], typical of the winter near-glacier dynamics. In this regime, the buoyant plume at the glacier front is composed of submarine melting and entrained ambient waters. The new water mass changes the ambient stratification near the glacier, which in turn alters the plume buoyancy forcing $B(z) \sim g'(z)Q(z)$, where $Q(z)$ is the depth-dependent plume volume flux, and consequently the plume vertical velocity $W_p(z) \sim B(z)^{1/3}$ [*Turner*, 1980]. The lower temperature below the PW/AW interface close to the glacier front reduces the plume buoyancy forcing and the plume vertical velocity (Figure 5d). The opposite happens above the interface where the temperature is higher than in the control simulation. Since the submarine melt rate parameterization depends on the plume temperature and velocity [*Holland and Jenkins*, 1999], lower (higher) plume temperature, and velocity below (above) the PW/AW interface produce a lower (higher) *smr* (Figure 5).

At depth, where the effects on the stratification of the new water mass intrusion are smaller, the changes in submarine melting and plume properties are reduced (Figure 4c, rows 1–4, note the different scales in Figure 4).

Even though the difference between the averaged-temperature profiles with and without the intermediary circulation is small (Figure 5b, red and black lines), its strong temporal variability (Figure 4, row 2) is crucial for the plume velocity. In particular, the change in stratification near the glacier reduces the vertical extent of the plume in the AW layer, in the region where W_p and *smr* are maximum. On the other hand, the changes in the plume in the PW layer occur in a region where W_p and *smr* are minimum. Hence, we observe a small *smr* increases in the PW layer and a large *smr* decreases in the AW layer with a net decrease of $\overline{smr}$

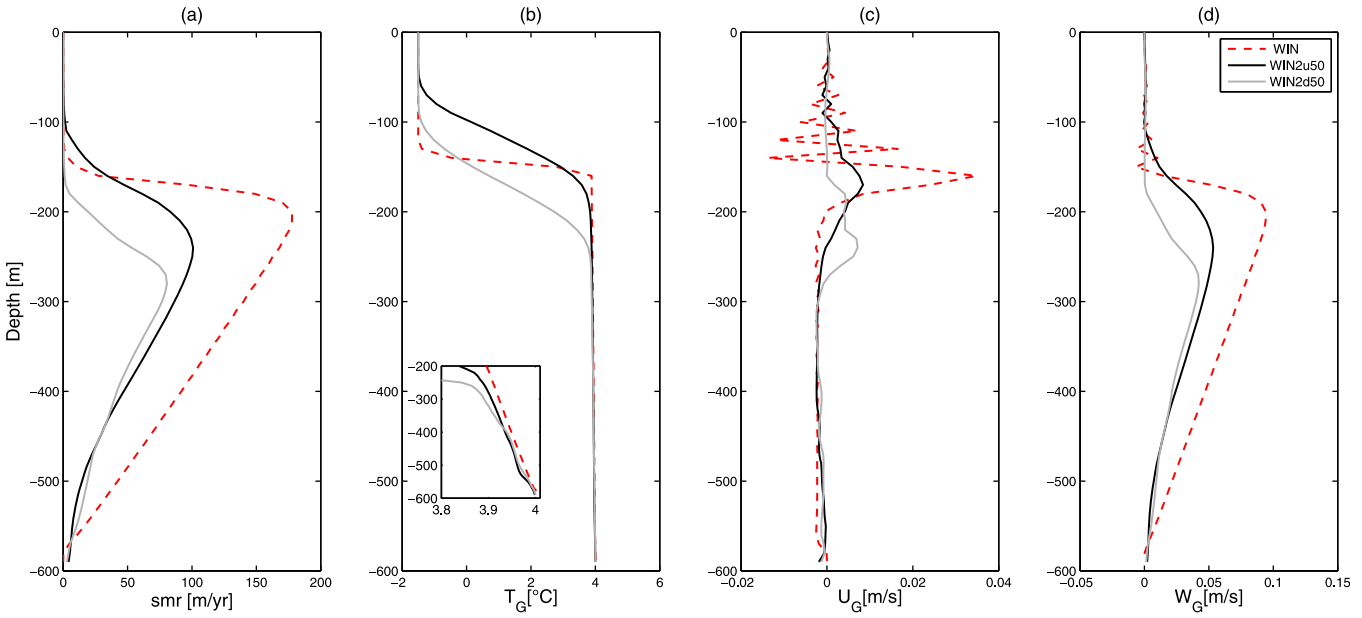

Figure 5. Winter regime. Time-averaged vertical profiles at the glacier front: (a) submarine melting, (b) temperature, (c) horizontal, and (d) vertical velocity as a function of depth. Black lines represent the winter reference simulation WIN2u50, gray solid lines the WIN2d50 simulation, and red-dashed lines the WIN control simulation. Note that the boundary conditions impose a zero horizontal velocity at the glacier front, hence U_G is the horizontal velocity within the buoyant plume, U_P.

averaged over the whole glacier depth. This nonlinear response of the plume dynamics to the change in stratification near the glacier front is the principal cause of the observed reduction in *smr*.

This nonlinear response is emphasized further in the downward sinusoidal simulations (WIN2d50). In this scenario, the new water mass generates an intrusion located mainly below the interface that reaches the glacier and further reduces the vertical extent of the plume in the AW layer and the velocity maximum at the glacier front (Figure 5d, gray solid line). This, in turn, influences the submarine melting distribution (Figure 5a, gray solid line). The averaged $\overline{smr}$ is 34 and 24 m yr^{-1} for the WIN2u50 and the WIN2d50 simulations, respectively. These values are smaller than the value of the control simulation (WIN) $\overline{smr}=70$ myr^{-1}.

Inside the fjord, 30 km away from the mouth, the raw horizontal velocity (Figure 6a) shows the density intrusion moving toward the glacier and the velocity field reconstructed from the first Empirical Orthogonal Function (EOF) shows a "pulses" pattern in response to the periodic forcing generating the intermediary circulation (Figure 6b). The first EOF captures 60% of the velocity variability. Furthermore, the Hovmöller diagram of the distance between the isotherm T_2 and T_1 shows that the new water mass, generated by the periodic density variations at the mouth of the fjord, travels inside the fjord and reaches the glacier front after ~130 h (white arrow Figure 6d), in good agreement with the predicted arrival time, $t_{\eta}=138$ h, of the intrusion (see section 4). The arrival of the intrusion at the glacier front at ~130 h is also shown by the increased distance between the isotherm T_2 and T_1 at the glacier front (dashed line in Figure 6c).

5.2. Summer (SUM2u50)

In summer, the buoyant plume at the glacier front is forced both by subglacial discharge and submarine melting and a "convection-driven melting" regime [*Motyka et al.*, 2003; *Jenkins*, 2011] describes the near-glacier dynamics. In this regime, subglacial discharge is the main buoyancy source of the plume with only a small contribution from submarine melting. The plume increases its temperature and flow rate by entrainment processes mostly below <400 m depth, where the effects on the stratification of the intrusion of the new water mass are reduced. The summer dynamics of a purely glacier-driven fjord circulation (for Qsg= 4.35 m^3 s^{-1}) is characterized by a vigorous plume of subglacial discharge, submarine melting, and entrained ambient waters that rises vertically at the glacier front and intrudes at the interface between the AW/PW layers [regime I, *Sciascia et al.*, 2013]. A less vigorous plume rises in the PW layer and leaves the glacier front at the free surface.

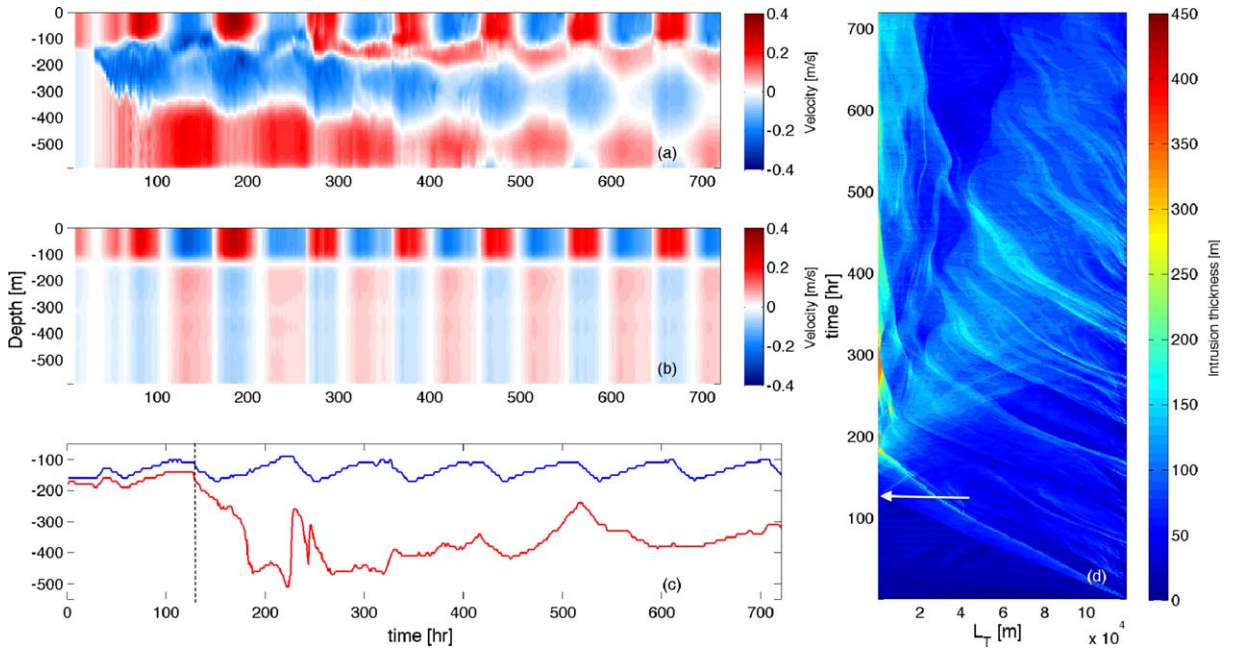

Figure 6. (a) Raw horizontal velocity 30 km away from the mouth of the fjord as a function of time and depth for the WIN2u50 simulation. Positive velocity corresponds to outflow (i.e., toward the fjord mouth), negative velocity to inflow (i.e., toward the glacier front). (b) First EOF multiplied by its principal component. (c) Depth of the isotherm T_2 (red line) and T_1 (blue line) at the glacier front as a function of time. (d) Hovmöller diagram of the distance between the isotherm T_2 and T_1 as a function of time and distance from the glacier.

The *smr* and plume properties in the AW layer are not significantly modified by the intermediary circulation and the arrival at the glacier front of the new water mass intruding inside the fjord (Figures 7b and 7c, rows 1–4). The time average of the submarine melting is approximately equal to the *smr* for the SUM simulation at the same depth (Figures 7b and 7c, row 1) because the subglacial discharge dominates the buoyancy flux of the plume and its dynamics. As discussed above, the intermediary circulation has a "thermodynamical" effect with the new water mass reaching the glacier without significantly altering the velocity distribution near the glacier front. For upward sinusoidal density variation, the new water mass near the glacier allows the plume in the AW layer to penetrate past the original location of the interface at −150 m. The vertical velocity, temperature, and consequently *smr* are therefore enhanced in the top 150 m (Figure 8). One should note that in the absence of intermediary circulation (Figure 8, red dashed line) the buoyant plume in the AW layer intrudes at the interface and the intrusion is ∼100 m thick affecting the temperature, velocity, and *smr* at a depth of 100 m (Figures 8). Contrary to the winter behavior (WIN2u50), the enhanced summer *smr* in the top 150 m is not counterbalanced by a reduced submarine melting in bottom 450 m (Figure 8a). Hence, the vertically averaged submarine melting $\overline{smr}$ is of the order of 782 m yr^{-1} which is slightly higher than the submarine melting $\overline{smr}$ = 738 m yr^{-1} observed in the SUM control simulation (Table 1). For downward sinusoidal forcings (SUM2d50), the new water mass near the glacier front leads to a reduction of the vertical extent of the plume in the AW layer, as discussed in section 5.1. This causes a reduction of the plume vertical velocities in the AW layer, and consequently of the submarine melting (Figure 8, gray solid lines) equal to $\overline{smr}$ = 716 m yr^{-1}.

Subglacial discharge is highly variable on seasonal to interannual timescales [*Andersen et al*., 2010; *Mernild et al*., 2010]. As the subglacial discharge varies throughout the summer season, the dynamics at the glacier front evolves into different regimes in which the buoyant plume either intrudes into the ambient waters at the AW/PW interface or at the free surface [see *Sciascia et al*., 2013, for a detailed description]. For all of the above dynamical regimes, we find a slightly higher $\overline{smr}$ for the upward sinusoidal density variation simulations compared to the equivalent control (SUM) simulation (not shown).

5.3. Influence of η and t_{IC} Variability

The effects of the forcing volume V_η and the time scale of the density variations on submarine melting and fjord dynamics are investigated by changing in winter (WINup) and summer (SUMup) the parameter η, both for upward and downward sinusoidal forcing, as well as the forcing time (t_{IC}).

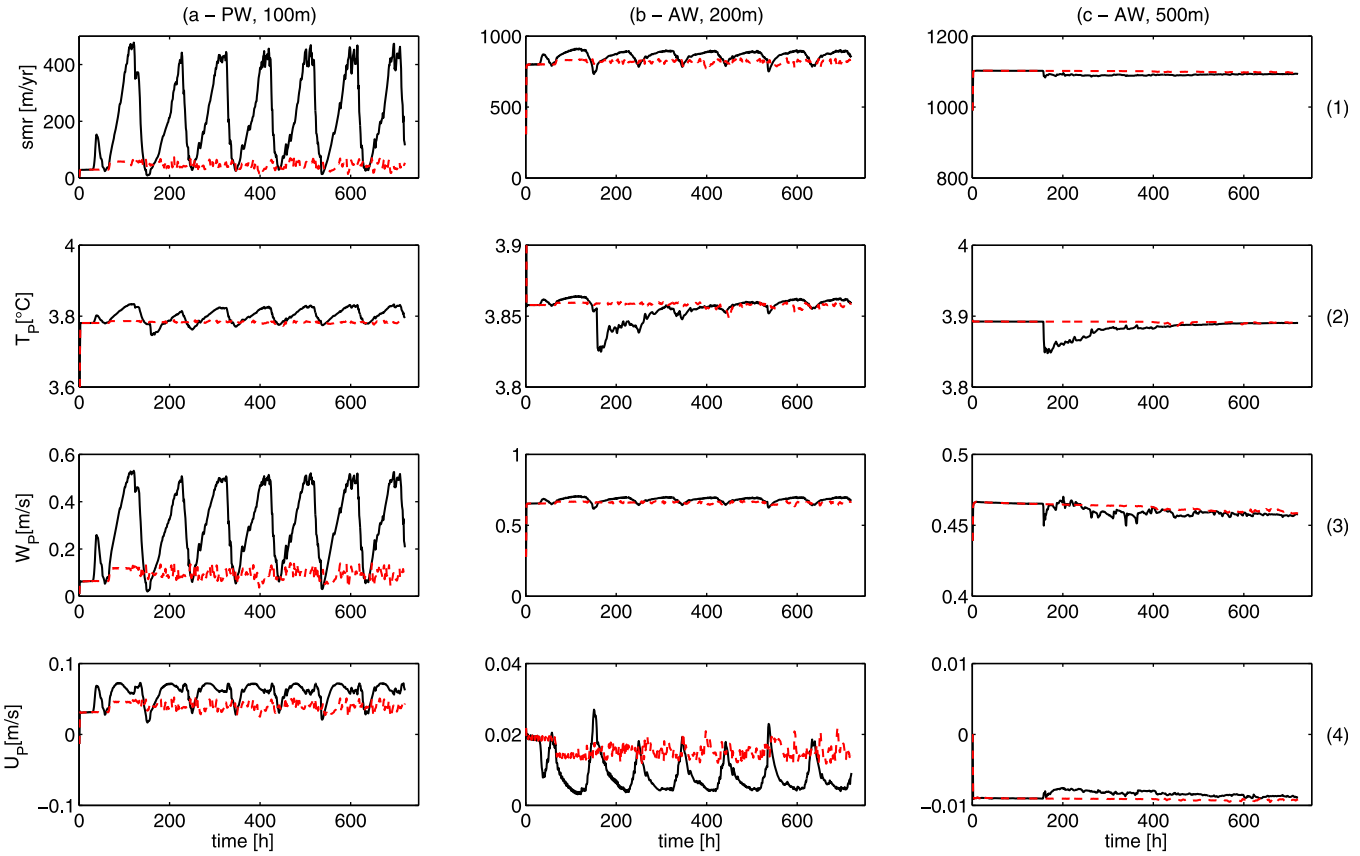

Figure 7. Same as Figure 4, but for the summer intermediary circulation.

To estimate the influence of the intermediary circulation on the $\overline{smr}$, the effect of the difference in thickness of the AW/PW layers needs to be removed. Hence, we introduce the ratio of $\overline{smr}$ over the $\overline{smr}_{\eta/2}$, the latter occurs in the absence of intermediary circulation when the depth of the AW layer is $H_2+\eta/2$. In the presence of an intermediary circulation, the AW layer depth would be $H_2+\eta/2$ in the extreme case in which the new water mass intrusion had properties equal to those in the AW layer and extended $\eta/2$ above the PW/AW interface (see section 4). In the absence of intermediary circulation, *Sciascia et al.* [2013] show, in both seasons, a linear dependence of $\overline{smr}$ on H_2, i.e., $\overline{smr}_{\eta/2}=A(H_2+\eta/2)+B$. The coefficients A and B, different for summer and winter simulations, are obtained from the glacier-driven circulation simulations in *Sciascia et al.* [2013]. If the variations in submarine melting observed in the presence of an intermediary circulation are due only to the variations in layers thickness, we expect $R=\overline{smr}/\overline{smr}_{\eta/2}$ to be equal to one.

Figure 9a shows that in winter not only R is not equal to one but it decrease with η. This can be explained as follows. The plume vertical velocity at the glacier front increases with height with a maximum at the AW/PW interface (Figure 5d). The intermediary circulation brings a new water mass to the glacier front. This in turn reduces the vertical extent of the plume in the AW layer, the plume maximum vertical velocity, and consequently the $\overline{smr}$ (see section 5.1). Taller intrusions generated by larger values of η, with averaged properties intermediate between those of the PW and AW, bring a larger volume of the new water mass toward the glacier than shallower intrusions, hence decreasing R with increasing η. In summer, on the other hand, the dynamics is strongly influence by subglacial discharge and we expect R to be closer to one. Figure 9b shows that the variations in $\overline{smr}$ are mainly due to the changes in layer thickness, i.e., $R\sim 1$. A small increase in R with η is due to the increased vertical extent of the plume in the AW layer, which induces a slightly higher plume vertical velocity and an increase in $\overline{smr}$ with η (Figures 8a and 8d). In neither season, there is a strong dependence of R on the forcing time (Figure 9).

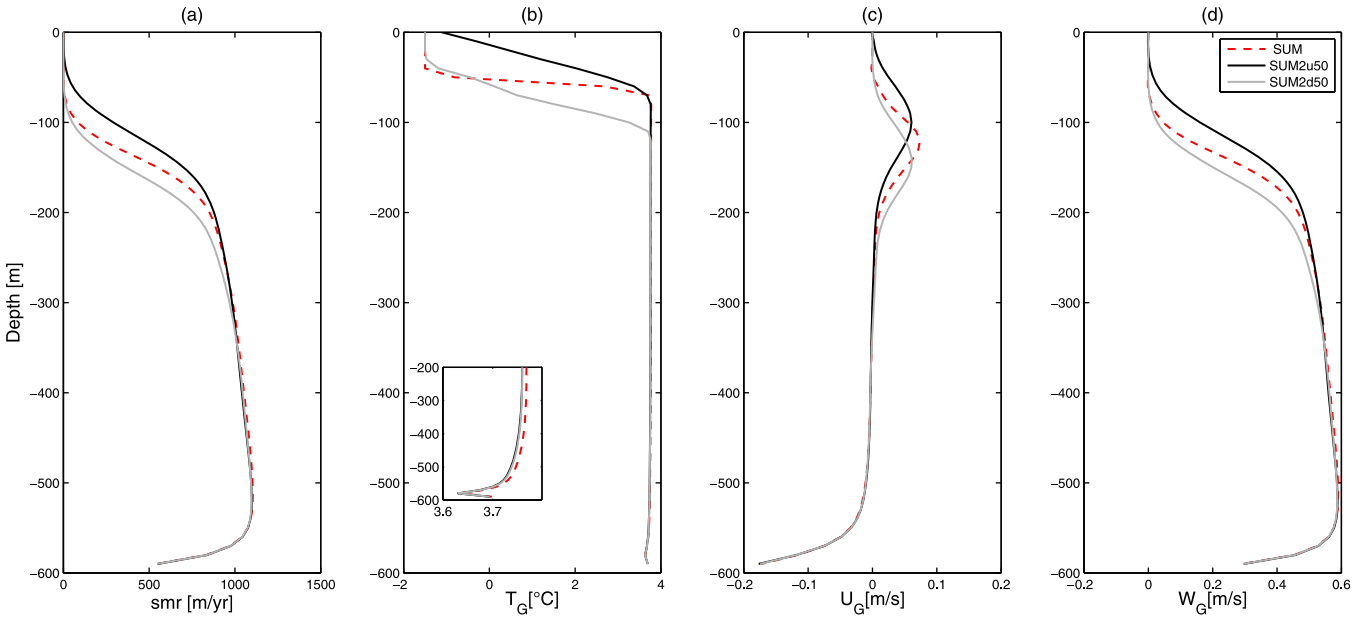

Figure 8. Same as Figure 5, but for the summer regime.

6. Laboratory Experiments Results: Top-Hat Forcing

6.1. Intermediary Circulation

The laboratory experiment starts by placing the ice block on the left side of the tank (Figure 3). The ice block is introduced in the tank very slowly and the amount of mixing between the two layers is very small. The solid block positioned on the opposite side of the tank then moves down and up every t_B generating a circulation in the tank. Figure 10a illustrates the evolution in time of the horizontal velocity, U, 30 cm away from the ice front in the upper layer (solid) and bottom layer (dashed) for $t_B = 24$ min (Experiment 2) after the solid block has moved toward the bottom of the tank. The lighter fluid in the top layer initially moves away from the ice front (positive velocities) while the denser fluid in the bottom layer moves toward the ice (negative velocities). After approximatively 45 s (red arrows in Figure 10a), the velocity reverses sign due to the reflection of the flow on the sides of the tank, the top layer moves toward the ice, and the bottom layer away from it. After approximately another 45 s, the flow approaches a state of rest until the next movement of the solid block. Due to the smaller thickness of the top layer, the velocity in this layer is larger than in the bottom layer.

The temperature evolution near the ice block is illustrated in Figure 10c, while Figure 10b shows the temperature anomaly with respect to the temperature obtained before the experiment started. After the ice block is positioned in the tank, the "melt-driven convection" regime [*Jenkins*, 2011] develops. A thin boundary layer of cold meltwater entrains ambient waters and rises until it reaches either the interface between the two layers, if in the bottom layer, or the free surface, if in the top layer. This circulation, previously observed in numerical studies [*Sciascia et al.*, 2013], is visible in Figure 10c where the temperature of the water below the interface (black solid line) and the free surface is cooling with time as the plume meltwater accumulates below the interface and the free surface. These results confirm that the meltwater mainly deposits within the interior of the water column and not entirely at the free surface. The intermediary circulation is visible in the temperature signal as an increase and decrease of the interface depth between the bottom layer and the meltwater layer (white line) every t_B. A thin layer of cold water is also visible near the bottom of the tank. This is a dense gravity current generated by the water in the bottom layer not entrained in the meltwater plume but cooled by the presence of the ice block, as previously observed by *Huppert and Josberger* [1980].

6.2. Influence of t_B on Submarine Melting

As expected, within the bottom 15 cm the submarine melting is maximum at ~5cm above the bottom (Figure 11a). This occurs because the meltwater plume slowly fills the entire tank and, as time progresses, a

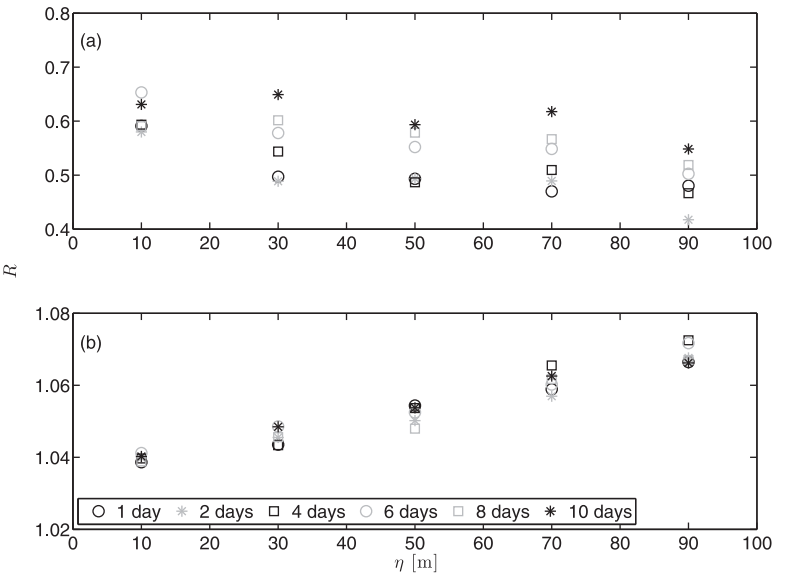

Figure 9. $R = \frac{\overline{smr}}{\overline{smr}_{\eta/2}}$ as a function of η for (a) winter simulations and (b) summer simulations. Different symbols correspond to different forcing times t_{IC}.

larger portion of the water column near the ice front is occupied by the cold meltwater instead of the warmer AW layer (Figure 10c). During the first 240 min, the location at 5 cm from the bottom (dashed black line in Figure 10c) is above the cold gravity current flowing along the bottom of the tank and below the plume meltwater accumulating below the interface, and it is approximately the location where the maximum temperature and submarine melting are observed (Figures 11a and 11b). Hence, the time averages have been performed over 240 min.

The submarine melting at 5 cm above the bottom does not vary substantially with the introduction of an intermediary circulation and it varies only slightly with t_B^* (Figure 12). The horizontal velocity, U, 30 cm from the ice front induced by the solid block movement decreases to zero within approximately 90 s (Figure

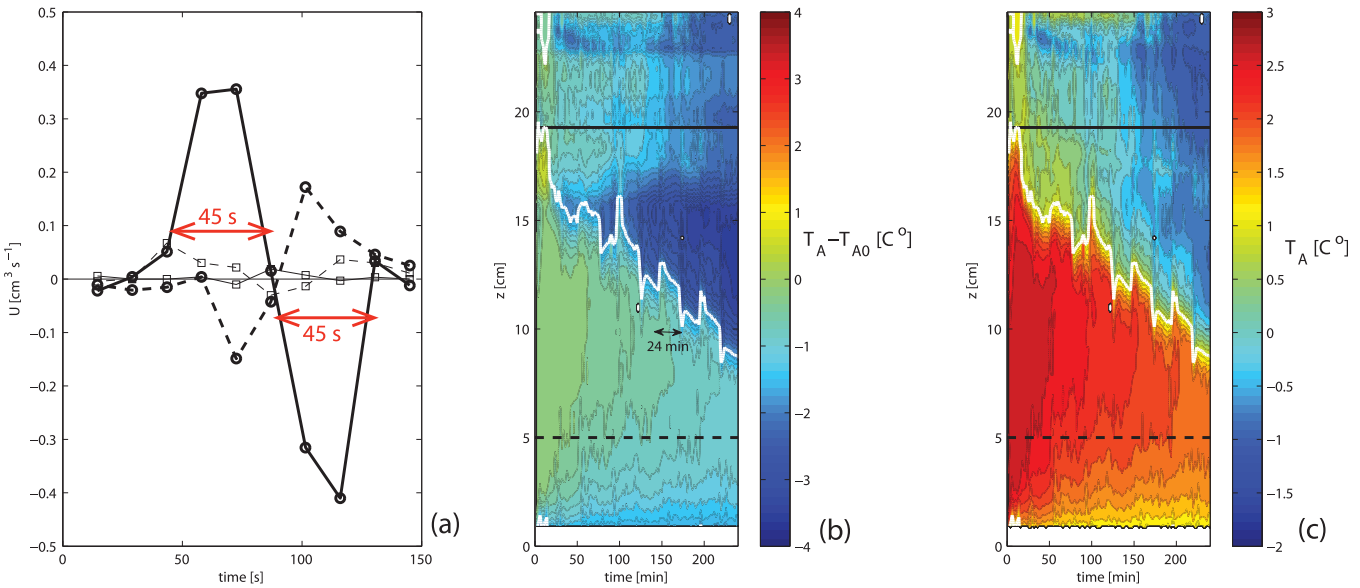

Figure 10. Laboratory results: (a) time evolution of the horizontal velocity, U, in the upper layer at $z = 22.4$ cm (solid thick line), and bottom layer at $z = 4.8$ cm (dash thick line) for $t_B = 24$ min (Experiment 2), after the solid block has moved toward the bottom of the tank. The velocity in the upper (lower) layer in the reference experiment (Experiment 1) with no forcing is shown by the thin solid (dashed) line. Time evolution of (b) temperature anomaly, $T_A - T_{A0}$, and (c) temperature T_A near the ice block for the same experiment as in Figure 10a. (b) Colors indicate the temperature difference between the temperature obtained at a time t and the temperature acquired before the experiment started. Black solid (dashed) line indicate the position of the interface (5 cm above the bottom), white line indicates the isotherm at $T_A = 1°C$. White areas indicate missing data.

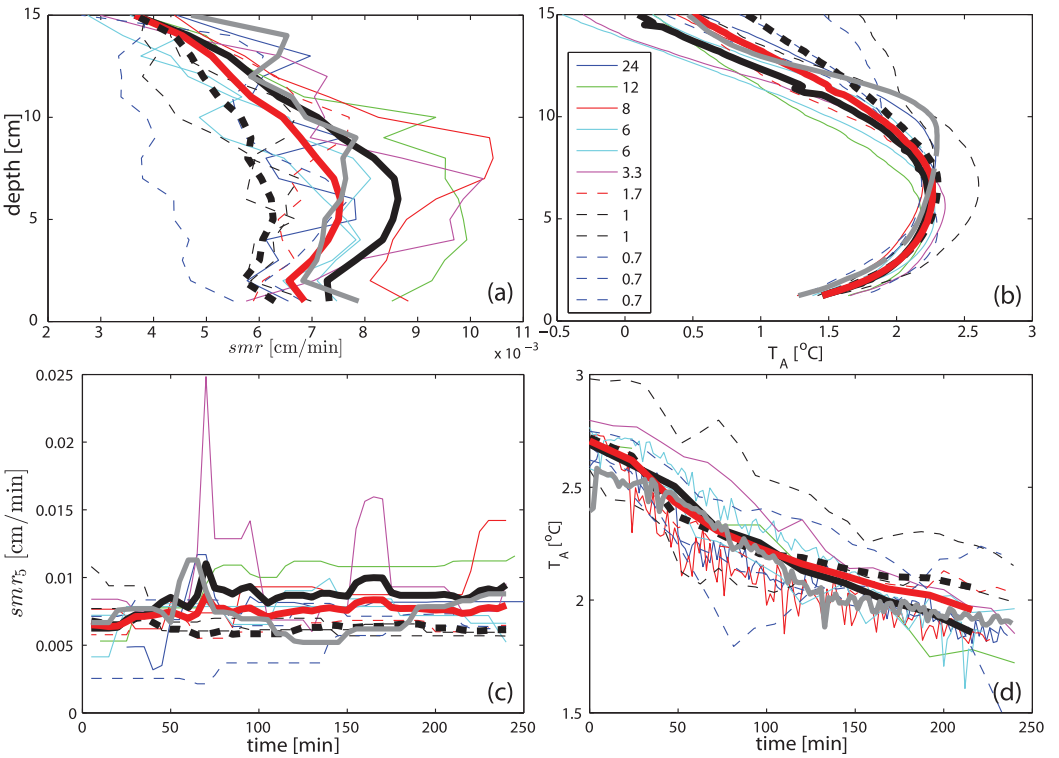

Figure 11. (a) Depth dependence of the ice submarine melting averaged over the first 240 min. (b) Depth dependence of the temperature at 2 cm from the ice block, T_A, averaged over the first 240 min. Time evolution of Figure 11c the ice submarine melting at 5 cm above the bottom and (d) the temperature at 2 cm from the ice block, T_A, at 5 cm above the bottom. Red thick line represents the average over all experiments, and solid (dashed) black thick line represents the average over the long (short) time experiments. Gray solid thick line indicates the reference experiment with no forcing (Experiment 1). The value of t_B (min) for the different lines is indicated in the legend.

10a). Hence, the experiments can be divided in those forced over times shorter than 100 s, i.e., $t_B^* \leq 1.0$, and those forced over longer times, i.e., $t_B^* > 1.0$, which will be referred to as "short time" and "long time," respectively.

Figure 12 suggests that the submarine melting for the long time experiments is slightly larger than that of the short time experiments and of the experiment with no forcing (srm_{WIN}), i.e., $s^* = smr/srm_{WIN} > 1$, albeit the difference is only marginal and within the observed maximum and minimum submarine melting. This result is confirmed when considering the submarine melting smr_5 over the first 240 min (Figure 11c). The long-time experiments (solid black thick line) show a larger submarine melting than the short time experiments (dashed black thick line) at all times after the first 30 min (Figure 11c). In particular, the submarine melting for the long-time experiments increases over the first hour, after which it remains constant. On the other hand, the submarine melting is approximately constant for the short-time experiments. The ice temperature increases during the first hour of the experiment (section 3), hence a slight increase in submarine melting is expected over the first hour.

The different submarine melting observed for the short-time and long-time experiments could be explained by the possible different water temperature in contact with the ice block when the forcing time is short compared to the time it takes for the velocity signal to return to zero. However, the evolution over the first 240 min of the temperature at 2 cm from the ice block, T_A, at 5 cm above the bottom (Figure 11d) suggests that all the experiments present approximately the same temperature near the ice.

In summary, the dynamical justification for the different submarine melting between the long-time and short-time experiments remains inconclusive. It is worth noting again that the signal is very small compared to its variability, hence the observed difference could be explained by the intrinsic variability of the data. Furthermore, the numerical model results suggest that in winter, small differences in the temperature at the glacier front are responsible for substantial changes in submarine

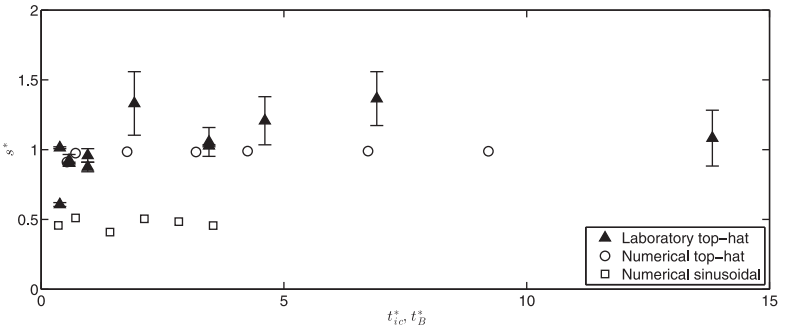

Figure 12. Nondimensional submarine melting, $s^* = smr/smr_{WIN}$, as a function of t^*_{IC} or t^*_B for the laboratory experiments (triangles) and for the numerical simulations with upward sinusoidal (squares) and top-hat (circles) forcings. The submarine melting for the laboratory experiments is computed at a depth of 5 cm above the bottom equivalent to a depth of 480 m for the numerical simulations. Multiple symbols for the same value of t^*_{IC} or t^*_B indicate repeated experiments. The maximum and minimum values of the laboratory submarine melting represent the error bars of the estimates (see section 3, for a detailed description).

melting. It is conceivable that the temperature measurements 2 cm away from the ice are not capturing the small differences responsible for the different submarine melting between the long-time and short-time experiments.

7. Model Results: Top-Hat Forcing

To investigate the role of a top-hat forcing similar to the one used in the laboratory experiments, we force the model with temperature and salinity values in the volume V_η at the mouth of the fjord that vary following the gray line in Figure 2. In the laboratory experiments, we consider the submarine melting at 5 cm from the bottom (see section 3). Hence, for the following analysis, we will only consider the submarine melting of the numerical simulations at the equivalent depth of 480 m.

Figure 12 shows the nondimensional submarine melting, $s^* = smr/smr_{WIN}$, for the laboratory experiments and the numerical simulations with a top-hat and a sinusoidal forcing as a function of the nondimensional forcing time. Provided that the forcing applied at the mouth of the fjord is equivalent, i.e., top-hat forcing, the numerical simulations (Figure 12, circles) and laboratory experiments (Figure 12, black triangles) are in good agreement and show small changes in submarine melting with t^*_B and compared to the WIN submarine melting, i.e., $s^* \sim 1$. On the other hand, the submarine melting for the numerical simulations, with a sinusoidal forcing is lower than in the winter control simulation (WIN) (Figure 12, squares). This result is also in agreement with one of the two laboratory experiments for which a continuous forcing, i.e., $t_F = 0$, has been applied (Figure 12, first triangle on the left).

It is worth noting that the ratio $R = \overline{smr}/\overline{smr}_{\eta/2}$ (see section 5.3) for the top-hat simulations varies between 0.8 and 0.9. These values are higher than those observed for the sinusoidal simulations (Figure 9a). Hence, the top-hat simulations have not only a higher local submarine melting at 480 m, but also a higher averaged melting over the entire glacier front.

The nonlinear response of the plume dynamics to the change in stratification near the glacier front (see section 5.1), occurs to a lesser extent also in the top-hat simulations, but only with a slight reduction in submarine melting compared to the WIN simulation (Figure 13). In particular, in the top-hat simulations, the new water mass at the fjord's mouth has properties closer to those of the AW layer and, as expected, the time-averaged profiles near the glacier (Figure 13, gray solid and dashed lines) are closer to those of the WIN simulation (Figure 13, red dashed line) than when a sinusoidal forcing is applied (Figure 13, solid black line). The profiles near the glacier deviates from the WIN experiments above approximately 350 m suggesting that the influence of the new water mass in the top-hat simulations does not influence the near-glacier dynamics at depth. The difference in submarine melting at $z = 480$ m and the ratio R observed when using two different forcing profiles (Figure 2) can be explained in light of the different averaged properties of the new water mass. With a sinusoidal forcing, the averaged water properties, e.g., temperature, are intermediate between those of the PW and AW, while with a top-hat forcing the averaged properties are closer to that of the AW. Hence, the temperature of the intrusion for a sinusoidal forcing is lower than for the top-hat forcing, inducing a lower submarine melting (Figure 14). When the boundary condition at the mouth of the fjord is sinusoidal (Figure 15, left), the new water mass that reaches the glacier front can penetrate deeper into the water column compared to the simulations with a top-hat forcing (Figure 15, right).

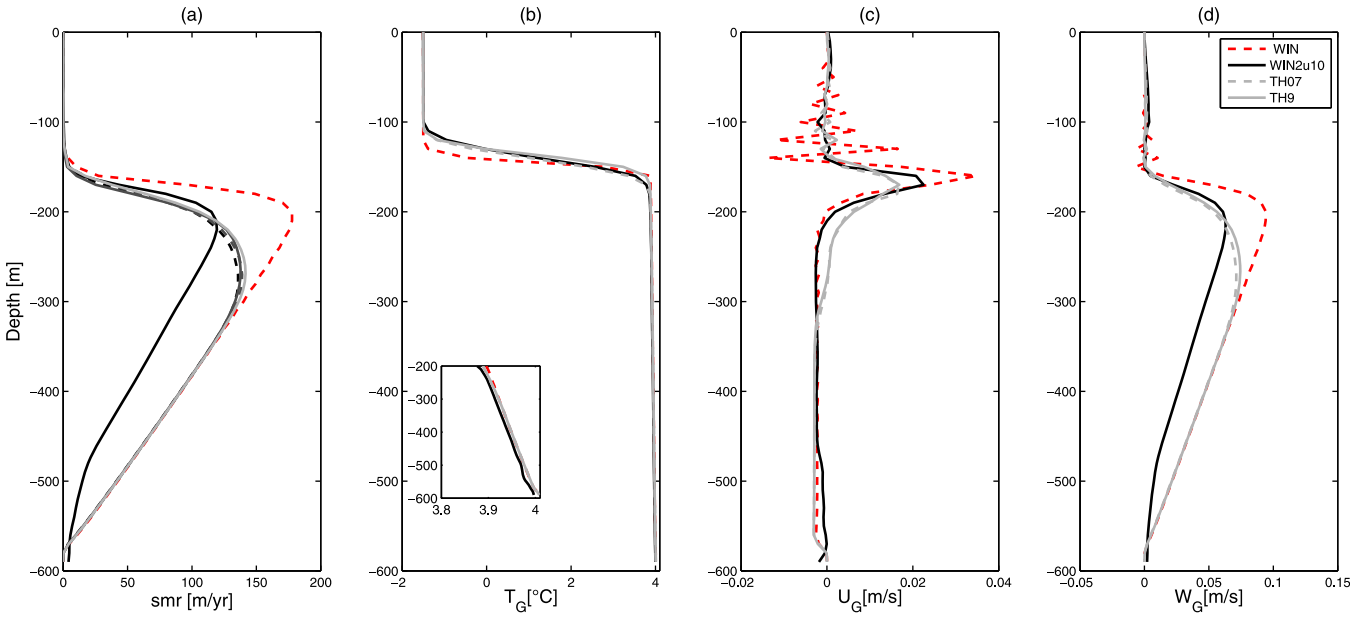

Figure 13. Top-hat simulations. Time-averaged vertical profiles at the glacier front: (a) submarine melting, (b) temperature, (c) horizontal, and (d) vertical velocity as a function of depth. Black lines represent the winter sinusoidal simulation WIN2u10, red-dashed lines the WIN control simulation, gray-dashed line the top-hat simulation with $t_B^*=0.7$, and gray solid line the top-hat simulation with $t_B^*=9$. Note that the boundary conditions impose a zero horizontal velocity at the glacier front, hence U_G is the horizontal velocity within the buoyant plume, U_P.

8. Summary and Conclusions

The impact of a periodic density variation at the mouth of a fjord on submarine melting of a vertical glacier front and fjord's dynamics is investigated using a nonhydrostatic ocean general circulation model and laboratory experiments. The setups are idealized representations of the Helheim Glacier/Sermilik Fjord system in southeast Greenland. The density variation at the fjord's mouth that generates an intermediary circulation can be induced by several processes on the continental shelf outside Sermilik Fjord, e.g., strong wind events, shear instabilities, and eddies. Although the production of a new water mass, at the mouth of Sermilik Fjord, with properties in between those of the AW and PW layers has not been observed yet, the above seem plausible mechanisms for the generation of a density variation upstream of the fjord. We performed numerical simulations investigating the submarine melting induced by a periodic density variation at the mouth of fjord using both a sinusoidal and top-hat forcing. These two forcings generate a new water mass with properties intermediate to those in the AW and PW layer and close to the bottom AW layer, respectively. The duration (i.e., t_{IC}) and magnitude (i.e., η) of the forcing were varied both in winter and summer

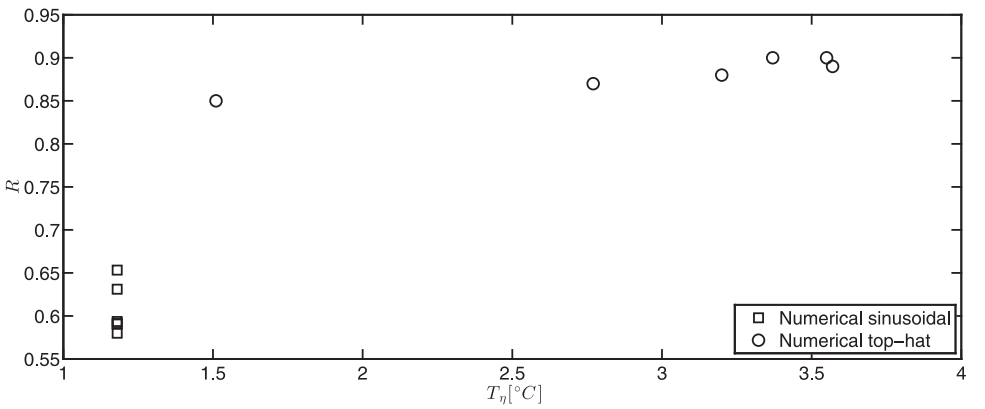

Figure 14. $R=\frac{\overline{smr}}{\overline{smr}_{\eta/2}}$ as a function of temperature of the intrusion T_η for numerical sinusoidal simulations (squares) with $\eta = 10$ m, and numerical top-hat simulations (circles). Different squares correspond to different forcing times t_{IC}.

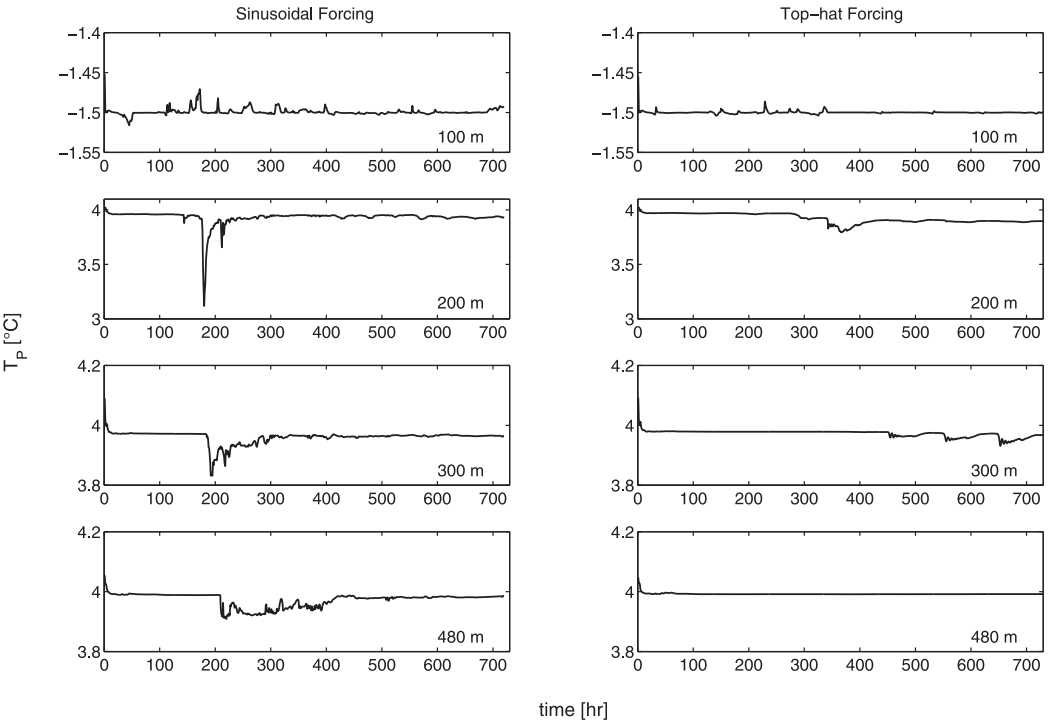

Figure 15. Plume temperature at different depths (100 m, 200 m, 300 m, 480 m) for a numerical simulation with a sinusoidal forcing (left) ($\eta/H_2=0.02$, $t_{IC}^*=0.35$) and with a top-hat forcing (right) ($\eta/H_2=0.02$, $t_B^*=0.71$).

conditions for the sinusoidal forcing, and only the duration (i.e., t_B) in winter condition for the top-hat forcing. The results compared to those obtained with a purely glacier-driven circulation.

The numerical results using a sinusoidal forcing indicate that the intermediary circulation has a "thermodynamical" effect on the dynamics, bringing, in both seasons, a new water mass near the glacier front, but with only a small effect on the velocity field near the glacier. In winter, when the near glacier dynamics is characterized by a "melt-driven convection" regime [*Jenkins*, 2011], the new water mass intrudes into the fjord and changes the ambient stratification near the glacier front. This in turn reduces the plume buoyancy forcing in the AW layer and results in a reduced submarine melting compared to a purely glacier-driven circulation.

In summer, on the other hand, the presence of subglacial discharge entering the fjord at depth dominates the near glacier dynamics, resulting in a "convection-driven melting" regime [*Motyka et al.*, 2003; *Jenkins*, 2011]. In this season, the intrusion of the new water mass near the glacier front slightly enhances the submarine melting by increasing the depth of penetration of the plume compared to a purely glacier-driven fjord circulation. On the other hand, for downward sinusoidal forcing, the depth of penetration of the plume is reduced, resulting in a slightly reduced $\overline{smr}$. Given the complexity of the laboratory apparatus, we chose not to perform the laboratory experiments in the summer regime with an intermediary circulation.

It is worth noting that although the variations in submarine melting induced by the intermediary circulation generated by a sinusoidal density variation at the mouth of the fjord (Figures 4 and 7) are small compared to those obtained in presence/absence of subglacial discharge, their contribution cannot be neglected when estimating the oceanic contribution to the glacier's submarine melting. The submarine melting is one order of magnitude larger in summer (738 m yr^{-1}) than in winter (70 m yr^{-1}), and this difference is largely due to the presence of subglacial discharge [*Sciascia et al.*, 2013]. However, the averaged (over all η and t_{IC}) changes in submarine melting induced by the intermediary circulation with sinusoidal forcing are of the order of $\sim$ 30 m yr^{-1} in winter, and $\sim$ 70 m yr^{-1} in summer. These values are comparable to those obtained by raising the temperature of the AW by 1°C from 4 to 5°C resulting in a $\sim$ 20 m yr^{-1} increase in $\overline{smr}$ in winter and 100 m yr^{-1} in summer.

The numerical results using a top-hat forcing are in good agreement with the results from the laboratory experiments using similar top-hat forcing, η^*, and t_B^*. Both numerical and laboratory submarine melting

measured at $z^* = 0.25$ from the bottom are similar to the submarine melting observed without an intermediary circulation. However, when the forcing applied at the mouth of the fjord is sinusoidal, the submarine melting decreases compared to the submarine melting of the winter control simulation (WIN) (Figure 12). This difference can be explained in light of the greater depths reached by the new water mass when a sinusoidal forcing is applied (Figure 15). Furthermore, the sinusoidal forcing generates a new water mass at the mouth with temperature intermediate between those of the PW and AW layers that causes a significant reduction in submarine melting, while with the top-hat forcing the new water mass has a temperature close to that of the bottom AW layer, and only a slight reduction in submarine melting is observed.

Using observations from Sermilik Fjord, *Jackson et al*. [2014] have shown a strong influence of the intermediary circulation on fjord dynamics, water distribution inside the fjord, and the transport of shelf properties to the upper fjord. The intermediary circulation in our study is forced by density variations at the mouth of the fjord and not by a displacement of the halocline driven by an upwelling/downwelling wind event, as observed in Sermilik Fjord [*Jackson et al*., 2014]. However, our results are in agreement with the findings in *Jackson et al*. [2014], and suggest that advection of shelf anomalies may occur via an intrusion with a velocity U_{II} that is an order of magnitude larger than the slow glacier-driven circulation in winter and more than twice as fast as the glacier-driven circulation in summer.

It is worth noting that in our simulations the properties of the new water mass at the fjord's mouth range between those inside the fjord. If the properties outside the fjord are different from those found inside the fjord, the characteristics of the new water mass advected by the intermediary circulation to the upper fjord at a much faster rate than a purely glacier-driven circulation [*Stigebrandt*, 1990; *Arneborg*, 2004; *Jackson et al*., 2014] can influence the submarine melting in a different way than observed in this study. This scenario is not considered here.

Despite the simplified nature of the numerical and laboratory setups, their comparison has proven to be useful to assess the relevant dynamics controlling the submarine melting and fjord circulation. However, potentially important dynamical features might have been neglected by assuming that the leading order dynamics is two-dimensional. Hence, the study of submarine melting and fjord circulation influenced by oceanic variability in a three-dimensional model with realistic bathymetry of Sermilik Fjord is the subject of ongoing research.

Acknowledgments
The authors would like to thank Lars Arneborg and Rebecca Jackson for their helpful comments on the manuscript. Support to C. Cenedese and F. Straneo was given by the National Science Foundation project OCE-1130008. C. Cenedese received support also from the WHOI Arctic Research Initiative. R. Sciascia and P. Heimbach are supported in part by NSF project OCE-1129746. Additional funding for P. Heimbach comes through NASA's project NNH11ZDA001N-IDS A.28. The data for this paper are available by contacting the corresponding author R. Sciascia (sciascia@mit.edu).

References

Adcroft, A., C. Hill, J. Marshall, and P. Heimbach (2004), Overview of the formulation and numerics of the MIT GCM, in *Proceedings of the ECMWF: Seminar Series on Numerical Methods, Recent Developments in Numerical Methods for Atmosphere and Ocean Modelling*, edited by ECMWF, pp. 139–149, Eur. Cent. for Medium-Range Weather Forecasts, Reading, U. K.

Andersen, M. L., et al. (2010), Spatial and temporal melt variability at Helheim Glacier, East Greenland, and its effect on ice dynamics, *J. Geophys. Res.*, *115*, F04041, doi:10.1029/2010JF001760.

Andreasen, J. (1985), Seasonal surface-velocity variations on a sub-polar glacier in West Greenland, *J. Glaciol.*, *31*, 319–323.

Arneborg, L. (2004), Turnover times for the water above sill level in Gullmar Fjord, *Cont. Shelf Res.*, *24*(4–5), 443–460, doi:10.1016/j.csr.2003.12.005.

Azetsu-Scott, K., and F. C. Tan (1997), Oxygen isotope studies from Iceland to an East Greenland Fjord: Behaviour of glacial meltwater plume, *Mar. Chem.*, *56*(3–4), 239–251.

Bamber, J., M. van den Broeke, J. Ettema, J. Lenaerts, and E. Rignot (2012), Recent large increases in freshwater fluxes from Greenland into the north Atlantic, *Geophys. Res. Lett.*, *39*, L19501, doi:10.1029/2012GL052552.

Benjamin, T. (1968), Gravity currents and related phenomena, *J. Fluid Mech.*, *31*, 209–248.

Catania, G. A., T. A. Neumann, and S. F. Price (2008), Characterizing englacial drainage in the ablation zone of the Greenland Ice Sheet, *J. Glaciol.*, *54*(187), 567–578.

Chu, V., L. Smith, A. Rennermalm, R. Forster, J. Box, and N. Reehy (2009), Sediment plume response to surface melting and supraglacial lake drainages on the Greenland Ice Sheet, *J. Glaciol.*, *55*(194), 1072–1082.

Dansereau, V., P. Heimbach, and M. Losch (2013), Simulation of sub-ice shelf melt rates in a general circulation model: Velocity-dependent transfer and the role of friction, *J. Geophys. Res.*, *119*, 1765–1790, doi:10.1002/2013JC008846.

Das, S. B., I. Joughin, M. D. Behn, I. M. Howat, M. A. King, D. Lizarralde, and M. P. Bhatia (2008), Fracture propagation to the base of the Greenland Ice Sheet during supraglacial lake drainage, *Science*, *320*(5877), 984–986.

Heimbach, P., and M. Losch (2012), Adjoint sensitivities of sub-ice-shelf melt rates to ocean circulation under the Pine Island Ice Shelf, West Antarctica, *Ann. Glaciol.*, *53*(60), 59–69.

Hellmer, H. H., and D. J. Olbers (1989), A two-dimensional model for the thermohaline circulation under an ice shelf, *Antarct. Sci.*, *1*(4), 325–336.

Holland, D. M., and A. Jenkins (1999), Modeling thermodynamic ice-ocean interactions at the base of an ice shelf, *J. Phys. Oceanogr.*, *29*(8), 1787–1800.

Holland, P. R., A. Jenkins, and D. M. Holland (2008), The response of ice shelf basal melting to variations in ocean temperature, *J. Clim.*, *21*(11), 2558–2572.

Howat, I. M., I. Joughin, and T. A. Scambos (2007), Rapid changes in ice discharge from Greenland outlet glaciers, *Science*, *315*(5818), 1559–1561.

Howat, I. M., I. Joughin, M. Fahnestock, B. E. Smith, and T. A. Scambos (2008), Synchronous retreat and acceleration of southeast Greenland outlet glaciers 2000–2006: Ice dynamics and coupling to climate, *J. Glaciol.*, *54*(187), 646–660.

Huppert, H., and E. Josberger (1980), The melting of ice in cold stratified water, *J. Phys. Oceanogr.*, *10*, 953–960.

Jackson, R. H., F. Straneo, and D. A. Sutherland (2014), Externally forced fluctuations in ocean temperature at Greenland glaciers in non-summer months, *Nat. Geosci.*, *7*, 503–508.
Jenkins, A. (1991), A one-dimensional model of ice shelf-ocean interaction, *J. Geophys. Res.*, *96*(C11), 20,671–20,677, doi:10.1029/91JC01842.
Jenkins, A. (2011), Convection-driven melting near the grounding lines of ice shelves and tidewater glaciers, *J. Phys. Oceanogr.*, *41*, doi:10.1175/JPO-D-11-03.1.
Klinck, J. M., J. J. O'Brien, and H. Svendsen (1981), A simple model of fjord and coastal circulation interaction, *J. Phys. Oceanogr.*, *11*(12), 1612–1626.
Losch, M. (2008), Modeling ice shelf cavities in a z coordinate ocean general circulation model, *J. Geophys. Res.*, *113*, C08043, doi:10.1029/2007JC004368.
Marshall, J., A. Adcroft, C. Hill, L. Perelman, and C. Heisey (1997a), A finite-volume, incompressible Navier-Stokes model for studies of the ocean on parallel computers, *J. Geophys. Res.*, *102*(C3), 5753–5766, doi:10.1029/96JC02775.
Marshall, J., C. Hill, L. Perelman, and A. Adcroft (1997b), Hydrostatic, quasi-hydrostatic, and nonhydrostatic ocean modeling, *J. Geophys. Res.*, *102*(C3), 5733–5752, doi:10.1029/96JC02776.
Mernild, S. H., G. E. Liston, I. M. Howat, Y. Ahn, K. Steffen, B. Hasholt, B. H. Jakobsen, B. Fog, and D. van As (2010), Freshwater flux to Sermilik Fjord, SE Greenland, *Cryosphere*, *4*, 453–465.
Moore, G. W. K., and I. A. Renfrew (2005), Tip jets and barrier winds: A QuikSCAT climatology of high wind speed events around Greenland, *J. Clim.*, *18*(18), 3713–3725.
Motyka, R. J., L. Hunter, K. A. Echelmeyer, and C. Connor (2003), Submarine melting at the terminus of a temperate tidewater glacier, LeConte Glacier, Alaska, USA, *Ann. Glaciol.*, *36*(1), 57–65.
Motyka, R. J., M. Truffer, M. Fahnestock, J. Mortensen, S. Rysgaard, and I. Howat (2011), Submarine melting of the 1985 Jakobshavn Isbræ floating tongue and the triggering of the current retreat, *J. Geophys. Res.*, *116*, F01007, doi:10.1029/2009JF001632.
Motyka, R. J., W. P. Dryer, J. Amundson, M. Truffer, and M. Fahnestock (2013), Rapid submarine melting driven by subglacial discharge, LeConte glacier, Alaska, *Geophys. Res. Lett.*, *40*, 5153–5158, doi:10.1002/grl.51011.
O'Leary, M., and P. Christoffersen (2013), Calving on tidewater glaciers amplified by submarine frontal melting, *Cryosphere*, *7*(1), 119–128, doi:10.5194/tc-7-119-2013.
Rignot, E., and P. Kanagaratnam (2006), Changes in the velocity structure of the Greenland Ice Sheet, *Science*, *311*(5763), 986–990.
Rignot, E., M. Koppes, and I. Velicogna (2010), Rapid submarine melting of the calving faces of West Greenland glaciers, *Nat. Geosci.*, *3*(3), 187–191.
Schjøth, F., C. S. Andresen, F. Straneo, T. Murray, K. Scharrer, and A. Korablev (2012), Campaign to map the bathymetry of a major Greenland fjord, *Eos Trans. AGU*, *93*(14), 141–142.
Schodlok, M. P., D. Menemenlis, E. Rignot, and M. Studinger (2012), Sensitivity of the ice-shelf/ocean system to the sub-ice-shelf cavity shape measured by NASA IceBridge in Pine Island Glacier, West Antarctica, *Ann. Glaciol.*, *53*(60), 156–162.
Sciascia, R., F. Straneo, C. Cenedese, and P. Heimbach (2013), Seasonal variability of submarine melt rate and circulation in an east Greenland fjord, *J. Geophys. Res.*, *118*, 2492–2506, doi:10.1002/jgrc.20142.
Shepherd, A., et al. (2012), A reconciled estimate of ice-sheet mass balance, *Science*, *338*(6111), 1183–1189, doi:10.1126/science.1228102.
Stearns, L. A., and G. S. Hamilton (2007), Rapid volume loss from two East Greenland outlet glaciers quantified using repeat stereo satellite imagery, *Geophys. Res. Lett.*, *34*, L05503, doi:10.1029/2006GL028982.
Stigebrandt, A. (1990), On the response of the horizontal mean vertical density distribution in a fjord to low-frequency density fluctuations in the coastal water, *Tellus, Ser. A*, *42*, 605–6014.
Straneo, F., and C. Cenedese (2014), Dynamics of Greenland's glacial fjords and their role in climate, *Annu. Rev. Mar. Sci.*, *7*(1), doi:10.1146/annurev-marine-010213-135133, in press.
Straneo, F., and P. Heimbach (2013), North Atlantic warming and the retreat of Greenland's outlet glaciers, *Nature*, *504*(7478), 36–43.
Straneo, F., G. Hamilton, D. Sutherland, L. Stearns, F. Davidson, M. Hammill, G. Stenson, and A. Rosing-Asvid (2010), Rapid circulation of warm subtropical waters in a major glacial fjord in East Greenland, *Nat. Geosci.*, *3*(3), 182–186.
Straneo, F., R. Curry, D. Sutherland, G. Hamilton, C. Cenedese, K. Vage, and L. Stearns (2011), Impact of fjord dynamics and glacial runoff on the circulation near Helheim Glacier, *Nat. Geosci.*, *4*(5), 322–327.
Straneo, F., D. Sutherland, D. Holland, C. Gladish, G. Hamilton, H. Johnson, E. Rignot, Y. Xu, and M. Koppes (2012), Characteristics of ocean waters reaching Greenland's glaciers, *Ann. Glaciol.*, *53*(60), 202–210.
Straneo, F., et al. (2013), Challenges to understand the dynamic response of Greenland's marine terminating glaciers to oceanic and atmospheric forcing, *Bull. Am. Meteorol. Soc.*, *93*(4), 485–498, doi:10.1175/BAMS-D-12-00100.
Sutherland, D. A., and F. Straneo (2012), Estimating ocean heat transports and submarine melt rates in Sermilik Fjord, Greenland, using lowered acoustic Doppler current profiler (LADCP) velocity profiles, *Ann. Glaciol.*, *53*(60), 50–58.
Sutherland, D. A., F. Straneo, and R. S. Pickart (2014), Characteristics and dynamics of two major Greenland glacial fjords, *J. Geophys. Res Oceans*, *119*, 3767–3791, doi:10.1002/2013JC009786.
Turner, J. (1980), *Buoyancy Effects in Fluids*, Cambridge Univ. Press, Cambridge, U. K.
van den Broeke, M., J. Bamber, J. Ettema, E. Rignot, E. Schrama, W. J. van de Berg, E. van Meijgaard, I. Velicogna, and B. Wouters (2009), Partitioning recent Greenland mass loss, *Science*, *326*(5955), 984–986.
Vieli, A., and F. Nick (2011), Understanding and modelling rapid dynamic changes of tidewater outlet glaciers: Issues and implications, *Surv. Geophys.*, *32*(4–5), 437–458.
Xu, Y., E. Rignot, D. Menemenlis, and M. Koppes (2012), Numerical experiments on subaqueous melting of Greenland tidewater glaciers in response to ocean warming and enhanced subglacial runoff, *Ann. Glaciol.*, *53*(60), 229–234.
Xu, Y., E. Rignot, I. Fenty, D. Menemenlis, and M. M. Flexas (2013), Subaqueous melting of store glacier, west Greenland from three-dimensional, high-resolution numerical modeling and ocean observations, *Geophys. Res. Lett.*, *40*, 4648–4653, doi:10.1002/grl.50825.
Zwally, H. J., W. Abdalati, T. Herring, K. Larson, J. Saba, and K. Steffen (2002), Surface melt-induced acceleration of Greenland Ice-Sheet flow, *Science*, *297*(5579), 218–222.